Josephson Ratchet Based on He-FIB Josephson Junction

EBERHARD KARLS UNIVERSITÄT TÜBINGEN

Physikalisches Institut

by

Alireza Jozani

Supervisor: Prof. Dr. Edward Goldobin

18. August, 2023

Acknowledgments

I would like to express my gratitude to my supervisor for introducing me to the subject, teaching me about it, and carefully reading my manuscript. Thanks to Christoph Schmidt for introducing me to the experimental setup and taking responsibility for producing our samples with He-FIB during my thesis. I give a heartfelt thanks to all others who helped me throughout my journey in my master's degree, especially Prof. Tumulka, for his unwavering dedication of time spent on me for general guidance.

Finally, I am deeply grateful to my parents for their invaluable support.

To my beloved parents

Contents

List of Tables

List of Figures

Introduction

Typically, when referring to a ratchet or, equivalently, Brownian motor, one can envision a system interacting with a surrounding large bath, where a particle moves in an asymmetric periodic potential (see the schematic Fig. 1). It has been demonstrated [2] that in such a system directed transport can be induced by unbiased driving forces with zero time average. This allows the particle to perform useful work under some specific conditions. The system can be driven by a stochastic perturbation, which, e.g., is caused by thermal noise. The effects of stochastic perturbations could be captured and studied.
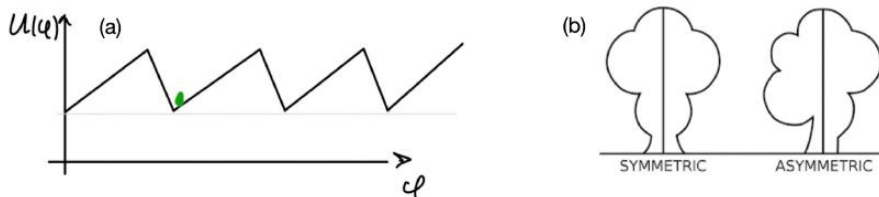
Figure 1: (a) An example of a particle trapped in a schematic asymmetric potential. (b) Schematically indicates the meaning of asymmetric.

This master's thesis focuses on the investigation of the Josephson ratchet based on High Temperature Superconductors (HTSs), namely YBCO, and fabricated using a Helium focused ion Beam (He-FIB) technique. Josephson junction of an in-line geometry is used to create the asymmetric potential. The Josephson ratchet is experimentally driven in both deterministic and stochastic regimes. Subsequently, we explored the effects of external and internal noises with a particular emphasis on the dominance of time-dependent perturbations.

As an **application**, the recent surge of interest is focused on superconducting diodes that can be used as the Josephson ratchets. For instance, reference [3] presents a notable realization of the diode, which is equivalent to a particle trapped in the Josephson asymmetric potential, as we will show later. However, in this thesis, we demonstrate that the Josephson ratchets generally exhibit higher efficiency and a smaller device footprint than those in ref. [3].

The thesis is organized as follows:

In Chapter 1 the concept of the Josephson effect with a 2π periodic gauge-invariant phase in the presence of a magnetic field is reviewed, with a specific focus on a particle trapped in a symmetric potential.

In Chapter 2 we theoretically investigate how a particle trapped in an asymmetric Josephson potential can be operated to generate useful work with a specific level of efficiency [1] [4]. Furthermore, the dependence of the critical current on the magnetic field is numerically simulated for the Josephson junction of an in-line geometry to gain initial insights into the required design parameters for a Josephson ratchet.

In Chapter 3 the focus shifts to the fabrication of the sample. The lithography process and irradiation techniques, such as He-FIB, are employed in the fabrication of the Josephson ratchet. Subsequently, we present the characterization of our samples.

In Chapter 4 we present the experimental investigation of two Josephson ratchets operating in two different regimes: deterministic (i.e., when the system is driven with a sinusoidal drive) and stochastic (i.e., when the Josephson ratchet is driven with a randomly varying signal, such as noise). We measure such characteristics as average voltage $\overline{V}_{\mathrm{dc}}$, output power $\overline{P}_{\mathrm{out}}$, input power $\overline{P}_{\mathrm{in}}$, and the efficiency. Since we operate in a quasi-static regime, we numerically calculate all the ratchet characteristics based on the experimental current-voltage characteristics. Furthermore, we investigate the effect of quasistatic noise on the rectification.

In conclusion we summarize our work and provide an **outlook** on future research directions.

Chapter 1

Josephson effect

1.1 Josephson Junction

The Josephson effect is a phenomenon that describes the flow of supercurrent, which is a current without dissipation, between two separated superconductors. When two superconductors, denoted as S_L and S_R, are brought close together with only a small gap (a barrier) separating them, a supercurrent can flow between them without any voltage applied. This device is known as a Josephson junction (JJ) and shown schematically in Fig. 1.1.
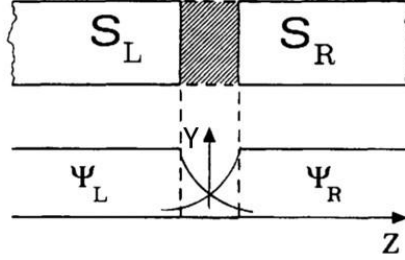
Figure 1.1: Schematic description of a Josephson junction, which is created by a barrier formed between two closely spaced superconductors on the left and right.

The left superconductor has a wave function of Cooper pairs (a pair of electrons or other fermions bound together at low temperatures) $\psi_L(t, \mathbf{x}) = |\psi_0| e^{i\phi_L(t,\mathbf{x})} = \sqrt{n_{s,L}} e^{i\phi_L(t,\mathbf{x})}$.[1] Similarly, the wave function for the right superconductor, S_R, is given by $\psi_R(t, \mathbf{x}) = |\psi_0| e^{i\phi_R(t,\mathbf{x})} = \sqrt{n_{s,R}} e^{i\phi_R(t,\mathbf{x})}$. If the potential difference across the junction is V, then the potential energy difference between the two superconductors is $2eV$, since each Cooper pair has twice the charge of an electron. The Schrödinger equation for these two quantum states, ψ_L and ψ_R, is as follows

$$i\hbar \frac{\partial}{\partial t} \begin{pmatrix} \sqrt{n_{s,L}} e^{i\phi_L} \\ \sqrt{n_{s,R}} e^{i\phi_R} \end{pmatrix} = \begin{pmatrix} eV & K \\ K & -eV \end{pmatrix} \begin{pmatrix} \sqrt{n_{s,L}} e^{i\phi_L} \\ \sqrt{n_{s,R}} e^{i\phi_R} \end{pmatrix}, \tag{1.1}$$

---

[1]Throughout this work, the bold symbols represent a three-dimensional vector.

where K is the coupling constant that represents the strength of the interaction between the wave functions of the two superconductors, $n_{s,i}$ (i = L or R) is the charge carrier density (Cooper pair density) which is proportional to the current I through the supercurrent density $\mathbf{j}_s = q_s \cdot n_s \cdot \mathbf{v}_s$, where $\mathbf{v}_s$ is the velocity vector of the Cooper pairs, q_s is the Cooper charge, and S_J is the surface area of the Josephson junction, which will be precisely defined once we define the geometry of JJ later in this chapter. After taking the derivative of eq. (1.1) and splitting the real and imaginary parts, we obtain the following set of equations for $\phi_L, \phi_R, n_{s,L}$, and $n_{s,L}$ [5]

$$\dot{n}_{s,L} = \frac{2K}{\hbar}\sqrt{n_{s,L}n_{s,R}}\sin\left(\phi_L - \phi_R\right),$$
$$\dot{n}_{s,R} = -\frac{2K}{\hbar}\sqrt{n_{s,L}n_{s,R}}\sin\left(\phi_L - \phi_R\right),$$

(1.2)

$$\dot{\phi}_L = \frac{K}{\hbar}\sqrt{\frac{n_{s,L}}{n_{s,L}}}\cos\left(\phi_L - \phi_R\right) + \frac{eV}{\hbar},$$
$$\dot{\phi}_R = \frac{K}{\hbar}\sqrt{\frac{n_{s,L}}{n_{s,L}}}\cos\left(\phi_L - \phi_R\right) - \frac{eV}{\hbar}.$$

(1.3)

The phase differences between two superconductors is defined as $\varphi_0 \equiv \phi_L - \phi_R$ (without presence of a magnetic field). Thus, the differences of $\dot{\varphi}_0 = \dot{\phi}_L - \dot{\phi}_R$ yields the 2nd Josephson equation as follows

$$\frac{\partial \varphi_0(t, \mathbf{x})}{\partial t} = \frac{2eV(t)}{\hbar} = \frac{2\pi V}{\Phi_0},$$

(1.4)

where $\Phi_0 = h/2e \approx 2.068 \times 10^{-15}$ Wb is magnetic flux quantum. Eq. (1.4) describes the linear evolution of phase differences across the junction for constant applied voltage. It immediately follows from eq. (1.4) that if there is no voltage across the junction, i.e., $V = 0$, then φ_0 is constant. This implies constant arguments of the angular functions in eq. (1.2), and thus $\dot{n}_{s,L} = -\dot{n}_{s,R}$. Therefore, if $n_{s,L} = n_{s,R}$, then $n_{s,i} = $ const, and the current should flow uniformly (in time) between the two superconductors. Otherwise, the superconductors would be charged, and the supercurrent would flow non-uniformly. Thus, the supercurrent density j_0 depends on the phase difference φ_0, which must be gauge invariant. That is, in the presence of the magnetic field, the supercurrent density becomes [2]

$$j_s(\psi) = q_s \operatorname{Re}\left\{\psi^*\left(\frac{\hbar}{mi}\nabla - \frac{q_s}{m}\mathbf{A}\right)\psi\right\} = \frac{q_s n_s \hbar}{m_s}\nabla\varphi,$$

where in the last equality we have inserted the definition of Cooper pair wave function and defined φ such as $\nabla\varphi := \nabla\varphi_0 - \frac{2\pi}{\Phi_0}\mathbf{A}$, which is the gauge invariant phase

---

[2]The Schrödinger equation implies the continuity equation $\left(\frac{\partial|\psi(t,\mathbf{x})|^2}{\partial t} = -\nabla \cdot j(t,\mathbf{x})\right)$, where the probability current density can be defined as $j_s(\psi)$. [6]

differences in the presence of magnetic field[3]. Now if we integrate this gauge invariant phase differences over the area of the barrier of the Josephson junction, we obtain

$$\varphi(t, \mathbf{x}) = \varphi_0 - \frac{2\pi}{\Phi_0} \int_L^R A_\mathrm{y}(\mathbf{x}) \, dx,$$

where A_y is a homogeneous magnetic vector potential in the y-direction perpendicular to the surface of JJ. Additionally, we note that inside the junction, $\psi(t, \mathbf{x})$ is defined modulo 2π $\left(\text{i.e.,} \psi(t, \mathbf{x}) = \sqrt{n_s} e^{i(\varphi(t,\mathbf{x})+2\pi)} = \sqrt{n_s} e^{i\varphi(t,\mathbf{x})}\right)$, so phase changes by $2n\pi$ (n is an integer) do not change the wave function ψ. Furthermore, $j_\mathrm{s}(\varphi)$ is time reversal invariant $\left(j_\mathrm{s}(\varphi) = -j_\mathrm{s}(-\varphi)\right)$.

Taking all these considerations into account, we define the uniform gauge invariant supercurrent density as an odd, 2π-periodic function of the phase difference, i.e., $j_\mathrm{s}(\varphi) = j_\mathrm{s}(\varphi + 2n\pi)$. This is so-called first Josephson equation, also known as supercurrent-phase relation, in the simplest case can be defined as

$$j_\mathrm{s} := j_0 \sin\left[\varphi(t, \mathbf{x})\right].$$

Assuming that the phase $\varphi(t, \mathbf{x})$ and the critical current density $j_0(\mathbf{x})$ are uniform (do not depend on $\mathbf{x}$), one can multiply the above equation by the area of the JJ barrier to obtain,

$$I_\mathrm{s} = I_0 \sin\left[\varphi(t)\right]. \tag{1.5}$$

This is the supercurrent, which flows between the two superconductors and is referred to as the Josephson supercurrent. In the eq. (1.5), I_0 is the maximum supercurrent that can flow through JJ and is known as the critical current. [8]

In a typical JJ experiment, we usually apply a current that flows through the JJ and then we measure the resulting output dc voltage. A commonly used electrical circuit model is called the Resistively and Capacitively Shunted Junction (RCSJ) model. This model assumes an equivalent circuit schematically depicted in Fig. 1.2.

---

[3]Here by gauge invariant phase we mean, e.g., that the expression $\nabla\varphi(t, \mathbf{x})$ will remain unchanged under using gauge transformations, that is, if we transform $\varphi_0(t, \mathbf{x}) \to \varphi_0(t, \mathbf{x}) + \frac{q_\mathrm{s}}{\hbar}\chi(\mathbf{x})$ and $\mathbf{A}(t, \mathbf{x}) \to \mathbf{A}(t, \mathbf{x}) + \nabla\chi(\mathbf{x})$, where $\chi(\mathbf{x})$ is any scalar field, we would see that the phase and subsequently supercurrent density will be invariant under these transformations. For more detail see the Ginzburg–Landau theory. [7]
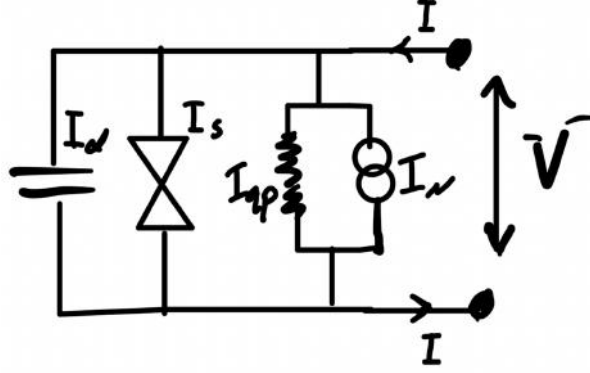
Figure 1.2: Schematic electronic equivalent circuit of JJ and a RCSJ model.

According to Kirchhoff's law, one can write the total current I coming from the current source as $I = I_d + I_{qp} + I_s + I_n$, i.e., it is divided into four components:

(I) The supercurrent $I_s = I_0 \sin[\varphi(t)]$;

(II) Dissipative (quasiparticle) current through the barrier $I_{qp} = V/R_N$; where R_N is a resistance of the barrier;

(III) Displacement current $I_D = C_J \dot{V}$; where C_J is a capacitance across junction;

(IV) At finite temperature T, the resistance simultaneously generates a thermal noise, which is represented by Johnson–Nyquist noise current source I_n parallel to the R in Fig. 1.2. It refers to the random fluctuations with Gaussian distribution that arise due to the thermal energy and agitation of the electrons in the resistance. This current is time dependent current with zero time average and with the dispersion given by

$$\sqrt{\langle i_n(t)^2 \rangle} = \sqrt{\frac{4k_B T \Delta f}{R}},$$

where Δf is the bandwidth of the system. We will investigate it experimentally later on in Chapter 4.

By neglecting the thermal noise sources, one can write

$$I = I_0 \sin[\varphi(t)] + \frac{V(t)}{R_N} + C_J \frac{dV(t)}{dt}, \tag{1.6}$$

which can be rewritten using eq. (1.4) via Josephson phase φ instead of V as

$$I = I_0 \sin(\varphi) + \frac{1}{R_N} \frac{\Phi_0}{2\pi} \dot{\varphi} + C_J \frac{\Phi_0}{2\pi} \ddot{\varphi}. \tag{1.7}$$

One can also derive the eq. (1.7) as the equation of motion (EoM) of a particle with coordinate φ moving in a potential energy $U(\varphi)$, using the Euler–Lagrange equation. The Josephson potential energy $U(\varphi)$ can be written as a cosinusoidal function

$$U(\varphi) \equiv E_J(1 - \cos\varphi - \gamma\varphi), \tag{1.8}$$

6

where $\gamma \equiv I/I_0$ represents the normalized bias current, and $E_{\mathrm{J}} \equiv I_0\Phi_0/2\pi$ is the so-called Josephson coupling energy. Fig. 1.3 illustrates the Josephson potential for different values of the γ. We observe that when $\gamma = 0$, the potential is mirror-symmetric (purple curve), and as γ increases, the potential becomes tilted. The shape of $U(\varphi)$ resembles an old-fashioned washboard, so it is referred to as a tilted washboard potential. It is evident that the tilt of the potential arises from γ. Specifically, the particle's phase motion on the purple, green, and red curves, where $0 \leqslant \gamma < 1$ may exhibit periodic oscillation. On the blue curve with $\gamma \geqslant 1$, however, the particle starts sliding down the potential and the particle's phase motion does not exhibit periodic oscillation [9].
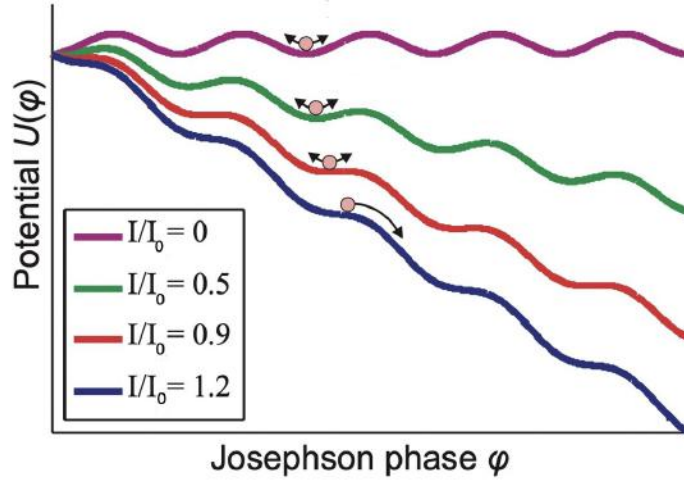
Figure 1.3: Plots of the tilted washboard potential $U(\varphi)$ are shown for several values of the tilt (bias current) γ. When $\gamma < 1$, the phase particle is trapped in the minimum of the potential. However, when $\gamma \geq 1$, the minima and barrier disappears and therefore the particle starts sliding down the potential.

It is often convenient to use normalize units, therefore we introduce a new normalized time

$$\tau \equiv \frac{t}{\tau_{\mathrm{c}}} = \frac{t}{2\pi e I_0 R}\Phi_0.$$

Then eq. (1.7) becomes

$$-\gamma + \sin\left[\varphi(\tau)\right] + \frac{d\varphi}{d\tau} + \beta_c\frac{d^2\varphi}{d\tau^2} = 0, \qquad (1.9)$$

where $\beta_c \equiv \dfrac{\omega_c^2}{\omega_p^2} = \dfrac{2\pi}{\Phi_0}I_0R_{\mathrm{N}}^2C$ is the so-called Stewart-McCumber parameter.

1.2 Current Voltage Characteristic (IVC)

Now let us see how a dc current-voltage characteristic (IVC) of the JJ looks like. In an experiment, we typically apply different values of the dc currents I and measure the average (dc) voltage across the junctions for each value of I, denoted as $\overline{V}(I)$. Using the known phase evolution $\varphi(t)$, which can be obtained by solving the eq. (1.9) for $\varphi(t)$, the average voltage can be calculated as follows

$$\overline{V}(I) = \frac{1}{T}\int_0^T V(t)dt \overset{(1.4)}{=} \frac{1}{T}\int_0^T \frac{\Phi_0}{2\pi}\frac{d\varphi}{dt}dt = \frac{1}{T}\frac{\Phi_0}{2\pi}\overbrace{\left[\varphi(T) - \varphi(0)\right]}^{2\pi} = \frac{\Phi_0}{T}. \qquad (1.10)$$

The parameter $T = \dfrac{2\pi}{\omega}$ represents the time it takes for a particle to complete one period of the potential shown in Fig. 1.3. Eq. (1.9) and (1.10) together can be used to obtain the typical IVC for different values of β_c as shown in Fig. 1.4.
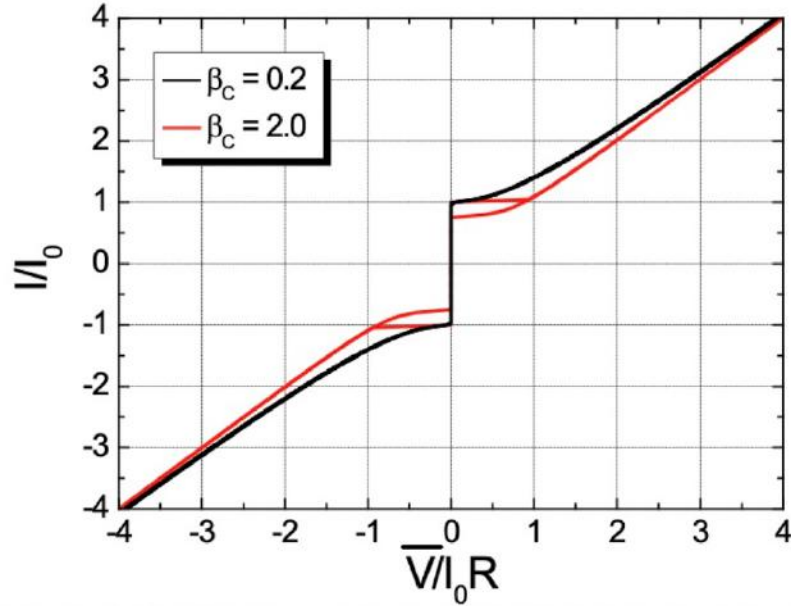
Figure 1.4: Current-Voltage Characteristic (IVC) for system with a symmetric potential.

For $\beta_c \ll 1$, where friction term $\dot{\varphi}$ dominates, one can neglect the last term $(\beta_c\ddot{\varphi})$ in the eq. (1.9). This leads to a non-hysteretic IVC, represented by the black curve in Fig. 1.4. In this case, one can determine the time it takes for the particle to complete one period of the tilted potential as

$$T = \frac{2\pi\tau_c}{\sqrt{\gamma^2 - 1}},$$

and calculate the averaged voltage,

$$\overline{V} = \begin{cases} I_0 R \sqrt{\gamma^2 - 1}, & \text{if } \gamma > 1, \\ -I_0 R \sqrt{\gamma^2 - 1}, & \text{if } \gamma < -1, \\ 0, & \text{otherwise.} \end{cases} \qquad (1.11)$$

For $\beta_c \gg 1$, the inertia term $\ddot{\varphi}$ in eq. (1.9) becomes dominant, resulting in a hysteretic IVC (the red curve in Fig. 1.4).

Since we are going to investigate YBCO junction where $\beta_c \ll 1$, the existence of thermal noise results in smearing of the critical current on experimental IVC. To quantify the smearing, we compare thermal energy $E_{\text{th}} = k_B T$ with the Josephson energy $E_J = I_0 \Phi_0 / 2\pi$ to find, for which value of the critical current $E_{\text{th}} = E_J$. From this, we can determine the typical value of the noise current as $I_{\text{th}} = 2\pi k_B T / \Phi_0$, for which the smearing of I_c is roughly equal to the I_c itself. The smearing effect occurs on the order of this thermal current, allowing us to conveniently characterize the degree of smearing using the normalized thermal current as follows [9]

$$\Gamma \equiv \frac{k_B T}{E_J} = \frac{2\pi k_B T}{I_0 \Phi_0} = \frac{I_{\text{th}}}{I_0}. \qquad (1.12)$$

To this end, we would like to highlight that the IVC is entirely symmetric. In other words, $\overline{V}(I) = -\overline{V}(-I)$.

1.3   Josephson Junction in a Magnetic Field

In the following, we will study the dependence of the IVC on the externally applied constant and uniform magnetic field, denoted as B. Specifically, we are interested in the dependence of $I_c(B)$. First, we will determine how the magnetic field affects the gauge invariant phase differences across the barrier JJ. Then, we will incorporate the phase differences across the JJ $\varphi(t, \mathbf{x})$ into the definition of the supercurrent density $j_s(\varphi)$. Finally, we will integrate it over the the area of JJ to obtain the total supercurrent over the junction, denoted as $I_s(B) = \int_{S_J} j_s(\varphi)\, d\mathbf{x}$. This $I_s(B)$ may take a range of values. Our objective is to determine the minimum or maximum value corresponding to I_c. Following [9], we assume that the field inside the barrier is arbitrary $B(x)$. Considering a JJ with a rectangular geometry for simplicity one can demonstrate that the magnetic field induces a gradient of phase differences φ given by

$$\frac{d\varphi}{dx} = \frac{2\pi}{\Phi_0} B(x) d_{\text{eff}}, \qquad (1.13)$$

where $d_{\text{eff}} = d + 2\lambda \tanh(d/\lambda)$ is the effective magnetic thickness of the barrier, d is the thickness of JJ, and λ is the London penetration depth. We assume that the magnetic filed B is applied along y-direction and therefore, $B(x)$ is along y-direction too, i.e., $B(x) \equiv B_y(x)\hat{y}$. Additionally, we observe that by the Ampère–Maxwell

equation, we have

$$\nabla \times B_{\mathrm{y}} = \frac{\partial B_{\mathrm{y}}(x)}{\partial x}\hat{z} = \mu_0 j_{\mathrm{z}}(x).$$

By taking derivative of eq. (1.13) with respect to x and using the Ampère–Maxwell equation, we obtain

$$\frac{\partial^2 \varphi(x)}{\partial x^2} = \frac{2\pi}{\Phi_0}d_{\mathrm{eff}}\frac{\partial B_{\mathrm{y}}(x)}{\partial x} = \frac{1}{\lambda_{\mathrm{J}}^2}\frac{j_{\mathrm{z}}(x)}{j_0} = \frac{1}{\lambda_{\mathrm{J}}^2}\sin\varphi(x), \tag{1.14}$$

where λ_{J} is so called the Josephson penetration depth[4], which is defined as follows

$$\lambda_{\mathrm{J}} \equiv \left(\frac{\Phi_0}{2\pi\mu_0 d_{\mathrm{eff}}j_0}\right)^{1/2}. \tag{1.15}$$

Eq. (1.14) defines $\varphi(x)$ in the absence of the bias current. For $B = 0$ the solution is $\varphi(x) = 0 \bmod 2\pi$. If $B > 0$, but small, according to eq. (1.13),

$$\left.\frac{d\varphi}{dx}\right|_{x=\pm L/2} = \frac{2\pi}{\Phi_0}Bd_{\mathrm{eff}},$$

then φ is also small. Thus, we can use Taylor expansion ($\sin\varphi \approx \varphi$) and solve eq. (1.14) to obtain $\varphi(x) = \varphi(0)e^{-x/\lambda_{\mathrm{J}}}$, i.e., λ_J determines the screening/penetration length of the magnetic field into the JJ. Now if we assume that our junction has length L smaller than Josephson penetration depth λ_{J}, then B fully penetrates into the JJ and becomes constant i.e., $B(x) \approx B$. Therefore, we consider a uniform magnetic field, which homogeneously penetrates into the JJ and allows us to take the integral of eq. (1.13) by pulling B out of the integral and obtain

$$\varphi(\mathbf{x}) = \varphi_0 + \frac{2\pi}{\Phi_0}Bd_{\mathrm{eff}}x. \tag{1.16}$$

Hence one can rewrite the eq. (1.5) as follows

$$I = \int_{S_J} j_{\mathrm{c}}(x,y)\sin\Big(\varphi(x)\Big)dx\,dy, \tag{1.17}$$

where $j_{\mathrm{c}}(x,y)$ is a critical current density, which can be uniformly (e.g., $j_{\mathrm{c}}(x,y) = $ const) or non-uniformly (e.g., $j_{\mathrm{c}}(x,y)$) distributed. Therefore, the critical current can be calculated by selecting a specific geometry and considering the presence of a magnetic field. The behavior of the supercurrent is investigated in [8] for various choices of current density and geometry. One can rewrite eq. (1.17) for a rectangular

---

[4]Notice that this calculation of λ_{J} is only valid for thick electrode e.g., $x > \lambda$. In the λ_{J} stays inductance which is equal to $\mu_0 d_{\mathrm{eff}}$ only if $d_{\mathrm{eff}} = 2\lambda$.

geometry of the JJ barrier $\left(\text{e.g., for a JJ with length } |x| \leqslant L/2 \text{ and width } W\right)$ as

$$I = W \int_{-L/2}^{L/2} j_{\mathrm{c}}(x) \sin{(\varphi)} dx = W \operatorname{Im} \left\{ e^{i\varphi_0} \int_{-L/2}^{L/2} j_{\mathrm{c}}(x) e^{i2\pi B d_{\mathrm{eff}} x / \Phi_0} dx \right\}. \qquad (1.18)$$

To obtain the maximum supercurrent, the eq. (1.18) should be maximized with respect to φ_0, i.e., we should find φ_0, for which $\left| \dfrac{dI}{d\varphi_0} = 0 \right|$. We obtain

$$I = W \left| \int_{-L/2}^{L/2} j_{\mathrm{c}}(x) e^{i2\pi B d_{\mathrm{eff}} x / \Phi_0} dx \right|. \qquad (1.19)$$

This is the maximum Josephson current at any given applied magnetic field B. If we assume a uniform critical current distribution i.e., $j_{\mathrm{c}}(x) = \text{const}$ inside the JJ, then the eq. (1.19) yields the well-known Fraunhofer dependence.

$$I_{\mathrm{c}}(\Phi_{\mathrm{J}}/\Phi_0) = I_0 \cdot \left| \frac{\sin{\left(\pi \dfrac{\Phi_{\mathrm{J}}}{\Phi_0}\right)}}{\pi \dfrac{\Phi_{\mathrm{J}}}{\Phi_0}} \right| = I_0 \cdot \left| \operatorname{sinc}{\left(\pi \frac{\Phi_{\mathrm{J}}}{\Phi_0}\right)} \right|, \qquad (1.20)$$

where $\Phi_{\mathrm{J}} = B d_{\mathrm{eff}} L$ is the total magnetic flux inside the junction and $I_0 = j_{\mathrm{c}} \times S_J = j_{\mathrm{c}} \cdot W \cdot L$. Eq. (1.20) can be rewritten for different polarities of current as

$$I_{\mathrm{c}\pm}(\Phi_{\mathrm{J}}) = \pm I_0 \cdot \left| \operatorname{sinc}{\left(\pi \frac{\Phi_{\mathrm{J}}}{\Phi_0}\right)} \right|, \qquad (1.21)$$

which can be plotted as shown in Fig. 1.5. The signs indicate maximum (I_{c_+}) and minimum (I_{c_-}) critical currents.
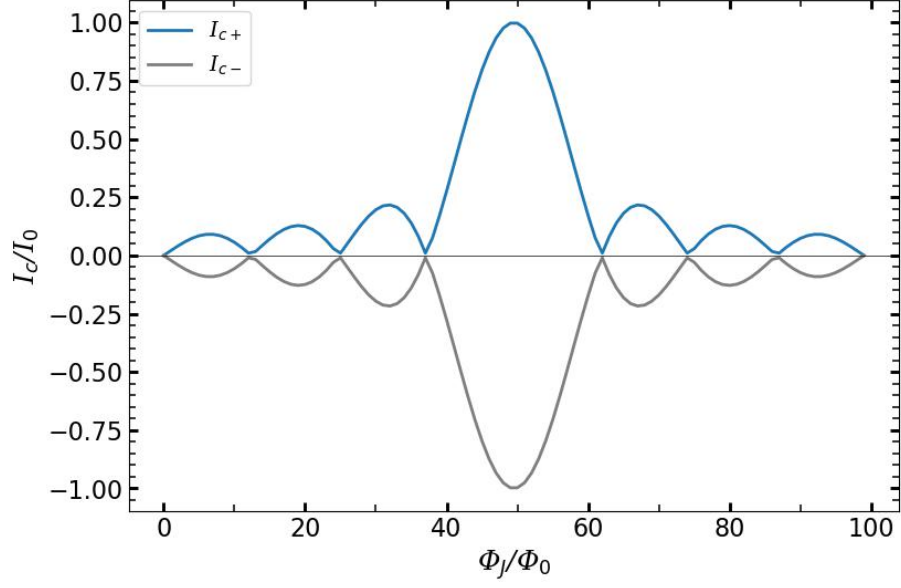
Figure 1.5: Negative and positive $I_c(\Phi_J)$ are symmetric for a fixed Φ_J. For example, when the value of Φ_J/Φ_0 is fixed at 44.5, we observe, $|I_{c_+}/I_0| = |I_{c_-}/I_0| = 0.75$.

Finally, we would like to point out that the $I_{c_\pm}(\Phi_J)$ curves are mirror symmetric with respect to the current polarity. In other words, for any fixed value of the flux Φ_J we find that $|I_{c_+}| = |I_{c_-}|$. [8]

Chapter 2

Theory of Ratchet

2.1 An Overview of Josephson Ratchet

When discussing a ratchet, the simplest model we have in mind is a periodic asymmetric potential[1] (see fig. 2.1 (a)), where a particle moves under the action of stochastic force with zero time average. Such a force pushes the particle back and forth, but on average, the force does not push the particle anywhere forward or backward. However, due to the asymmetry of the potential, in some cases, one can observe a net transport in a particular direction. Consequently, the random force with zero time average can be transformed into directed particle motion, enabling the particle to perform useful work. We will delve further into this concept in the subsequent sections of this chapter.

Since we will consider Josephson system in this thesis, the particle will move in the potential along the coordinate φ. Therefore, the averaged velocity $\langle \dot{\varphi} \rangle$ of the particle, is proportional to the averaged voltage, as described by eq. (1.4). Similarly, when we mention the application of current, as indicated in eq. (1.7), it is analogous to applying a force.[2] Hence, when we mention the application of a dc current to the system, it is synonymous with applying dc forces.
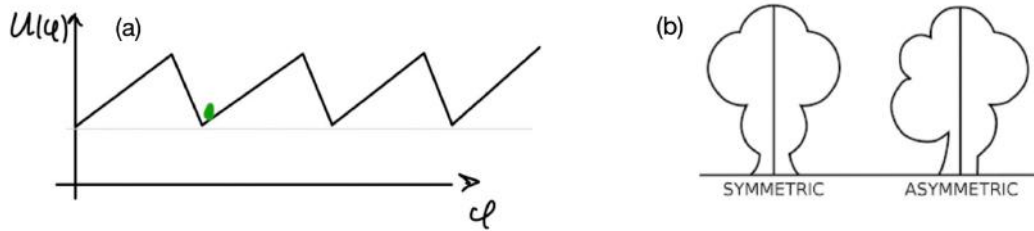
Figure 2.1: (a) An example of a particle trapped in a schematic asymmetric potential. (b) Schematically indicates the meaning of asymmetric.

---

[1]by asymmetrical, we mean reflexion asymmetry, $U(-\varphi) \neq U(\varphi)$.

[2]The Newtonian force for a stationary potential can be written as $F = -\nabla_\varphi U(\varphi)$. Now if we use the Josephson potential eq. (1.8), we would get $F \propto \gamma$, which means that applied current is proportional to force.

So far, we have studied the symmetric Josephson potential in detail, as seen in eq. (1.8), and Fig. 1.3. However to construct a Josephson ratchet, we need to design an asymmetric Josephson potential. We schematically show this kind of potential in Fig. 2.1(a).

Similar to Chapter 1.1, in order to determine the IVC, one can derive the dependence of the averaged voltage on the current from an EoM analogous to eq. (1.9), but this time for an asymmetric Josephson potential instead of symmetric potential. A non-hysteretic IVC for the asymmetric potential is schematically depicted in Fig. 2.2.
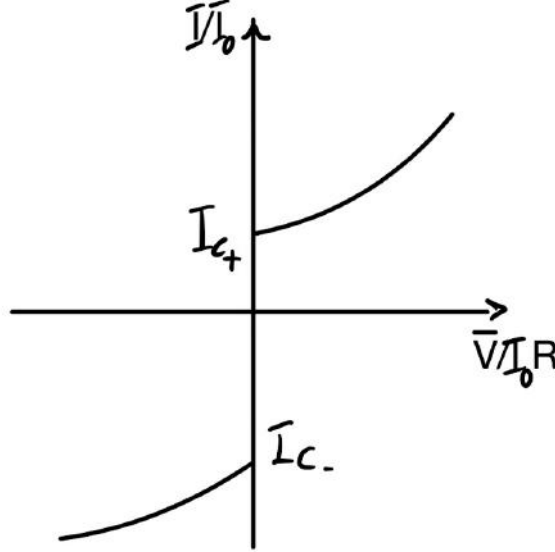
Figure 2.2: The schematic example shows an asymmetric non-hysteretic IVC for an asymmetric Josephson potential. I_{c_+} represents the positive critical current, and I_{c_-} represents the negative critical current.

We clearly observe that $|I_{c_-}| \neq |I_{c_+}|$, resulting in an asymmetric IVC, which is in contrast to what we obtained for the symmetric Josephson potential. This inequality in I_c values is attributed to the fact that in the asymmetric potential, the maximum slopes of the potential in the left/right directions are different. Therefore, the force (applied current) needed to overcome this slope (critical current) is also different for each polarity. We can now quantify the degree of asymmetry by using the symmetry parameter $\mathscr{A}$. This parameter is generally defined as the ratio of the maximum slopes of the potential in the left and right directions, i.e., by the ratio of critical currents

$$\mathscr{A} \equiv \frac{\max\left(|I_{c_+}|, |I_{c_-}|\right)}{\min\left(|I_{c_+}|, |I_{c_-}|\right)}, \quad 1 \leq \mathscr{A} < \infty. \tag{2.1}$$

Later, we will see that $\mathscr{A}$ is one of the key parameters defining the performance of the ratchet.

2.1.1 Josephson Ratchet Operation

If the IVC is similar to the our characteristic shown in Fig. 2.2, it is possible to construct a rectifier. Typically, a rectifier is operated by applying an ac signal $I(t) = I_{ac} \sin \omega t$ and measuring a dc output signal. In our specific case, we apply an ac current and observe the ratchet effect through the dc voltage response. This effect can be represented using a rectification curve $\overline{V}_{dc}(I_{ac})$. Fig. 2.3 schematically illustrates typical rectification curve.
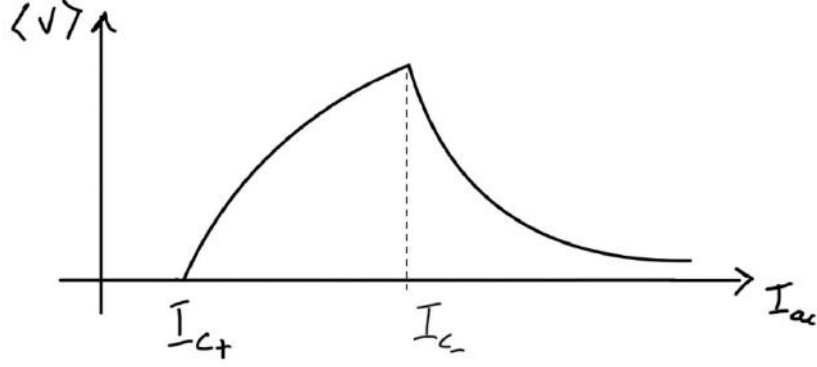
Figure 2.3: A rectification curve represents the average velocity of a particle ($\langle \dot{\varphi} \rangle \propto V$) as a function of the applied ac-drive amplitude I_{ac}. The interval between I_{c_+} and I_{c_-} is called operation interval or the rectification window, which can be defined as $\Delta \equiv I_{c_-} - I_{c_+}$.

When an alternating current is applied, it can be understood as tilting the potential back and forth at a frequency of ω. However, for small tilting amplitudes $I_{ac} < |I_{c_-}|$, we find that the particle remains trapped within the potential well, resulting in an average velocity (voltage) equals to zero. For $I_{ac} > |I_{c_+}|$, the particle starts moving forward in average with certain velocity (average voltage) $\overline{V}_{dc} > 0$. By further increases I_{ac}, average voltage increases until it reaches its maximum average velocity at $I_{ac} \rightarrow |I_{c_-}|$. As I_{ac} increases further, the average voltage gradually decreases until it eventually approaches zero. This happens because, during positive semi-period of ac-drive, the particle moves many periods in the easy direction, while during the negative semi-period of ac-drive, the particle also moves many periods in the difficult direction. Since, for a large amplitude of the drive, the slope caused by ac-drive is much larger than the slope of the potential, the potential's slope does not play a main role. As a result, the rectification is very small. The range between I_{c_+} and I_{c_-} is known as the rectification window (RW), representing the interval where the particle moves during a fraction of the positive semi-period of the drive and does not move (remain trapped) during the negative semi-period of the ac-drive.

We observe that a larger asymmetry parameter results in a wider RW. In the absence of asymmetry (i.e., in the case of a symmetric Josephson potential with $\mathscr{A} = 1$ or $|I_{c_+}| = |I_{c_-}|$), the rectification curve (average velocity) remains zero, and

the particle does not move in average. This occurs because the net time average force exerted on the particle from both left and right sides of the symmetric potential well is zero.

A relevant question arises: How good is a ratchet? How can we characterize its performance? Obviously, we want a ratchet to work not only for a certain amplitudes of the input signal, but for a very wide range of amplitudes, ideally from a small amplitude to a very large amplitude. However, as we saw in Fig. 2.3 the ratchet does not move for the small and very large amplitudes, and there is only a limited range of amplitudes (the RW), in which the rectification occurs ($\langle V \rangle \neq 0$). Therefore, to achieve a broad operational range for the ratchet, we aim to maximize the size of the RW. This entails minimizing $|I_{c_+}|$ and maximizing $|I_{c_-}|$. Consequently, a larger asymmetry parameter $\mathscr{A}$ leads to an expanded interval of operation, enabling a wider range of amplitudes in which the ratchet can function effectively.

However, even if the ratchet is capable of rectification, it does not yet generate useful work or deliver rectified power to a load. We refer to such a ratchet as being idle. To prevent the ratchet from being idle, we should load it i.e., by applying counterforce, typically in the form of a dc current I_{dc}. This counterforce tilts the potential and pushes the particle in the opposite direction to the ratchet motion. If the ratchet effect is stronger than this counterforce, the particle overcomes the constant (counter) slope and ascend, thereby performing useful work. Fig. 2.4 schematically depicts a loaded ratchet.
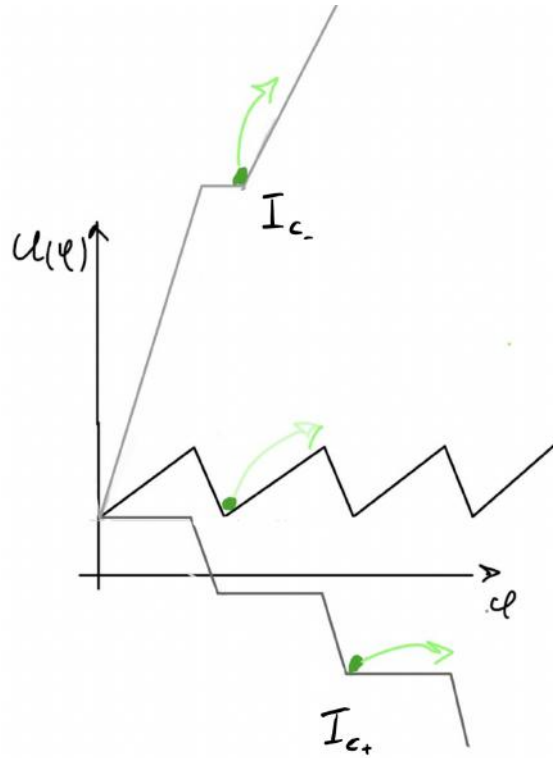
Figure 2.4: A ratchet potential for $I_{dc} = 0$, I_{c_-}, I_{c_+}.

If the countercurrent becomes too large, the ratchet stops (or even moves backwards in average) for any driving amplitude I_{ac}. We refer to such a current as the stopping current or stopping force. As illustrated in Fig. 2.4, if the ratchet transport initially occurs in the positive direction along the φ-axis, we apply $I_{\text{dc}} < 0$. This results in a potential tilt of $-I_{\text{dc}} \cdot \varphi$, compelling the particle to climb up due to the ratchet effect and perform useful work.

The rectification curve for a loaded ratchet is schematically depicted in Fig. 2.5.
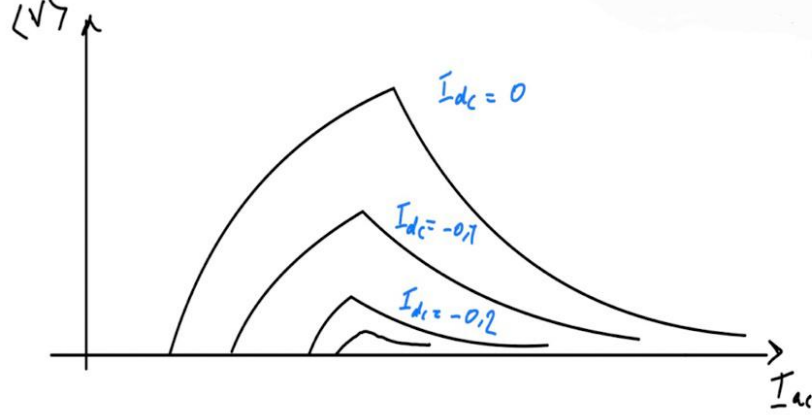
Figure 2.5: The schematic loaded ratchet up to countercurrent $|I_{\text{dc}}| = 0.2\,\mu\text{A}$.

It is evident that gradually increasing the load $|I_{\text{dc}}|$ leads to a reduction in the size of the rectification window and the values of $\overline{V}_{\text{dc}}$. This reduction shows that the ratchet is not strong enough for arbitrary I_{ac}. Specifically, we observe that as the load $|I_{\text{dc}}|$ increases, the operational range in terms of I_{ac} decreases. However, in this narrower interval, the particle is compelled to move against the ratchet motion and produce output power. Our primary objective is to maximize both the rectification windows (RWs) and the value of the stopping current.

To summarize this section, let us consider an example simulation of a ratchet that was studied in [1] and [4]. The simulations were conducted in a quasistatic regime, allowing for the acquisition of information about the ratchet's operation solely from its asymmetric IVC. The authors generated a step-like asymmetric IVC, as shown in Fig. 2.6(a), and simulated various figures of merit based on this asymmetric IVC. Fig. 2.6(b) presents the simulation results for a loaded rectification curve $\overline{V}_{\text{dc}}$.
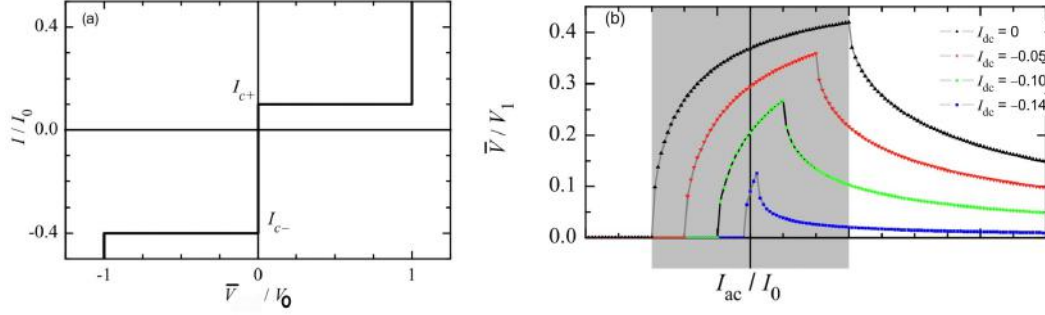
Figure 2.6: (a) A custom-made asymmetric IVC with $\mathscr{A} = 4$. (b) The rectification curves for several values of I_{dc} based on the asymmetric IVC, borrowed from [1].

The black curves in Fig. 2.6(b) correspond to the case where $\mathscr{A} = 4$ and $I_{dc} = 0$. By loading the ratchet and increasing I_{dc} (colored curves), we observe that the rectification window (RW) becomes smaller. However, within this shorter interval, the particle can perform more useful work and achieve higher efficiency, as we will explain in the following subsection.

2.1.2 Efficiency

Efficiency is defined as useful output dc power $\overline{P}_{out}$ divided by the total input power consumed by the system $\overline{P}_{in}$

$$\eta \equiv \frac{-\overline{P}_{out}}{\overline{P}_{in}}. \tag{2.2}$$

As a case study, the efficiency of the model investigated in [1] is presented in Fig. 2.7(e). The black curve represents the idle ratchet, while the colored curves correspond to loaded ratchets with different values of $|I_{dc}|$. The ratchet operates with maximum efficiency η at the beginning of the RW for any counterforce, as shown in Fig. 2.7(e). Furthermore, we notice that increasing $|I_{dc}|$ results in a smaller operation interval but a higher efficiency. In [4], it was demonstrated that the maximum efficiency achievable in principle is determined solely by the asymmetry of the potential and is given by

$$\eta_{max} = \frac{I_{c_-} - I_{c_+}}{I_{c_-} + I_{c_+}}.$$

Overall, we see that a higher asymmetry leads to a higher maximum efficiency.
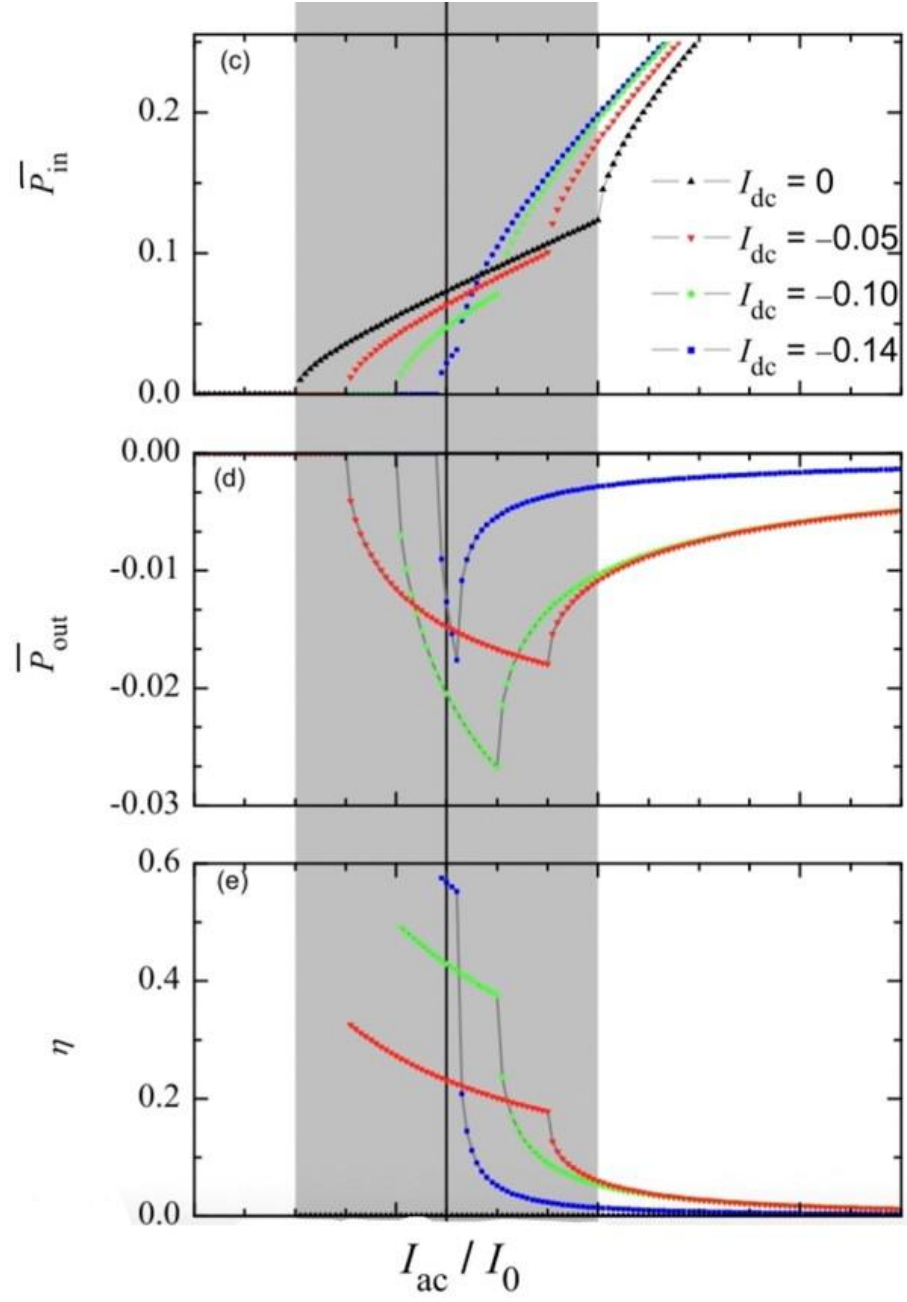
Figure 2.7: (c) Average input ac power $\overline{P}_{\text{in}}$. (d) Average output dc power $\overline{P}_{\text{out}}$. (e) Efficiency η, fig(4) of [1].

19

2.1.3 Junctions of In-line Geometry

In the classical textbook on the Josephson effect [8], Barone *et al.* considered an in-line JJ geometry, as shown in Fig. 2.8(a). In this geometry, the bias current fed from the right side flows through the Josephson barrier (the dashed hatched region) and produces the so-called self-field. Lets denote the current flowing through the top electrode with $I_L(x)$. We now assume that the maximum supercurrent corresponds to the uniform current flows across the Josephson barrier with the current density j_{c0}. By solving the continuity equation

$$\partial_x\left(\frac{I_L}{d}\right) = j_{c0}$$

with the boundary conditions $I_L(-L/2) = 0$ and $I_L(L/2) = I_0$, we obtain the current in the top electrode as

$$I_L(x) = j_{c0}d\left(x + \frac{L}{2}\right).$$

By solving Maxwell equation $\overrightarrow{\nabla} \times H_s = j_L(x)$, where $j_L(x) = I_L(x)/(wd)$, we obtain

$$H_s(x) = \frac{j_{c0}}{w}\left(\frac{x^2}{2} + \frac{Lx}{2}\right).$$
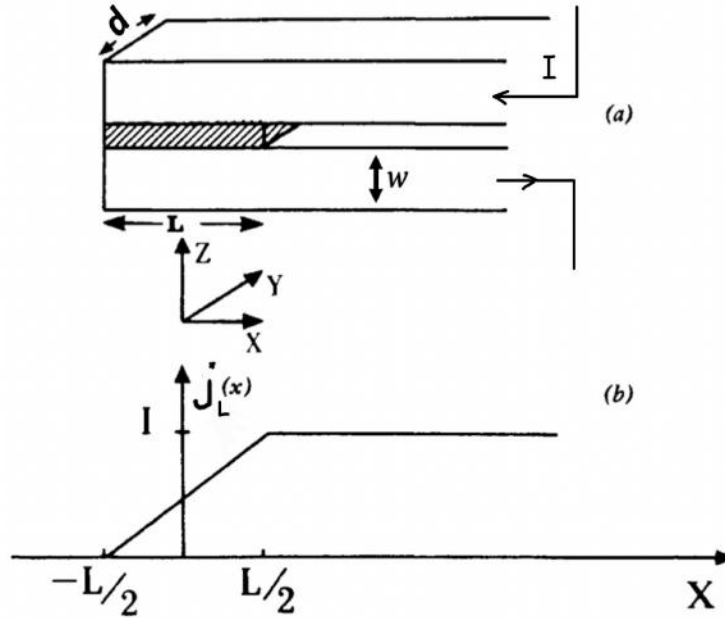
Figure 2.8: (a) The in-line geometry of a (JJ) consists of superconducting material where the dashed line represents the barrier JJ between superconductors. The arrows indicate the current I flowing through the superconductors and JJ. (b) The current density j_L as a function of distance x.

Following [8], we substitute this field profile by its average value

$$\overline{H}_s = \frac{5 j_{c0} L^2}{12 w} = \frac{5 I_0 L}{12 w d}, \tag{2.3}$$

which represents the self-field when we apply the maximum supercurrent $I = I_0$ through the junction. If we apply arbitrary I, then the self-field is given by $\overline{H}_s(I) = \overline{H}_s I / I_0$. The self-field together with the applied external magnetic field H_e gives a total field $H = H_e + H_s$. The maximum Josephson current through Josephson junction as a function of H is given by (see eq. (5.1.4) of the book [8])

$$I_c(H_e) = d L j_{c0} \left| \frac{\sin \left(\frac{\mu_0 \pi d_{eff} L}{\Phi_0} H \right)}{\left(\frac{\mu_0 \pi d_{eff} L}{\Phi_0} H \right)} \right|, \tag{2.4}$$

for small junction compared to Josephson penetration depth. One can rewrite the eq. (2.4) in terms of normalized fluxes as follows

$$\frac{I_c(f)}{I_0} = \left| \frac{\sin \pi \left(f + f^M \frac{I_c(f)}{I_0} \right)}{\pi \left(f + f^M \frac{I_c(f)}{I_0} \right)} \right|, \tag{2.5}$$

where $I_0 = d L j_{c0}$ is the maximum value of supercurrent I. We have defined normalized flux $f \equiv \Phi_J / \Phi_0$, where $\Phi_J = d_{eff} L H_e$ is the total applied flux inside JJ. The length of the JJ is denoted by L, and the effective magnetic thickness d_{eff} is given by $d_{eff} = 2 \lambda_{eff} \tanh(w / \lambda_{eff})$. Here, λ_{eff} is the effective London penetration depth, defined as $\lambda_{eff} = \lambda \coth(d/\lambda)$, where λ is the London penetration depth.

It is important to note that the Josephson penetration depth for the in-line geometry in this case differs from the eq. (1.15) in terms of magnetic thickness for the geometry shown in Fig. 2.8. The Josephson penetration depth here is given by,

$$\lambda_J \equiv \left(\frac{\Phi_0}{2\pi \mu_0 d' j_{c0}} \right)^{1/2}, \tag{2.6}$$

where $d' \mu_0$ is called specific inductance of electrode, and $d' = 2 \lambda_{eff} \coth(w / \lambda_{eff})$ for our in-line geometry. Additionally, we introduce $f^M \equiv \Phi_s^M / \Phi_0$ as the geometric normalized flux, where Φ_s^M describes the strength of the in-line geometry. It is determined by the eq. (2.4), and the definition of the self-field given in eq. (2.3), as follows

$$\Phi_s^M = \mu_0 \overline{H}_s d_{eff} L = \frac{5 \mu_0 L^2 d_{eff} I_0}{12 d w}. \tag{2.7}$$

Φ_s^M describes the effect of self-field. We can express f^M in terms of the Josephson penetration depth λ_J using the following equation

$$f^M = \frac{5L^3 d_{\text{eff}}}{24\pi\lambda_J^2 w d'}. \tag{2.8}$$

At $f^M = 0$, the maximum supercurrent $I_c(f)$ is symmetric Fraunhofer pattern $I(f) = I(-f)$ as given by the eq. (1.20) as shown in Fig. 1.5. Eq. (2.5) defines an implicit function of I_c on the flux f, which requires numerical solutions. We have developed a Python script that uses the bisection method to solve eq. (2.5) numerically. We then calculate $I_c(f)$ for several fixed values of f^M as presented in Fig. 2.9. One can see that $I_c(f)$ is skewed and the skewness of $I_c(f)$ depends on f^M. Visually, if we draw a vertical line at a fixed value of f, it becomes evident that $|I_{c_+}| \neq |I_{c_-}|$ for most of the f values.
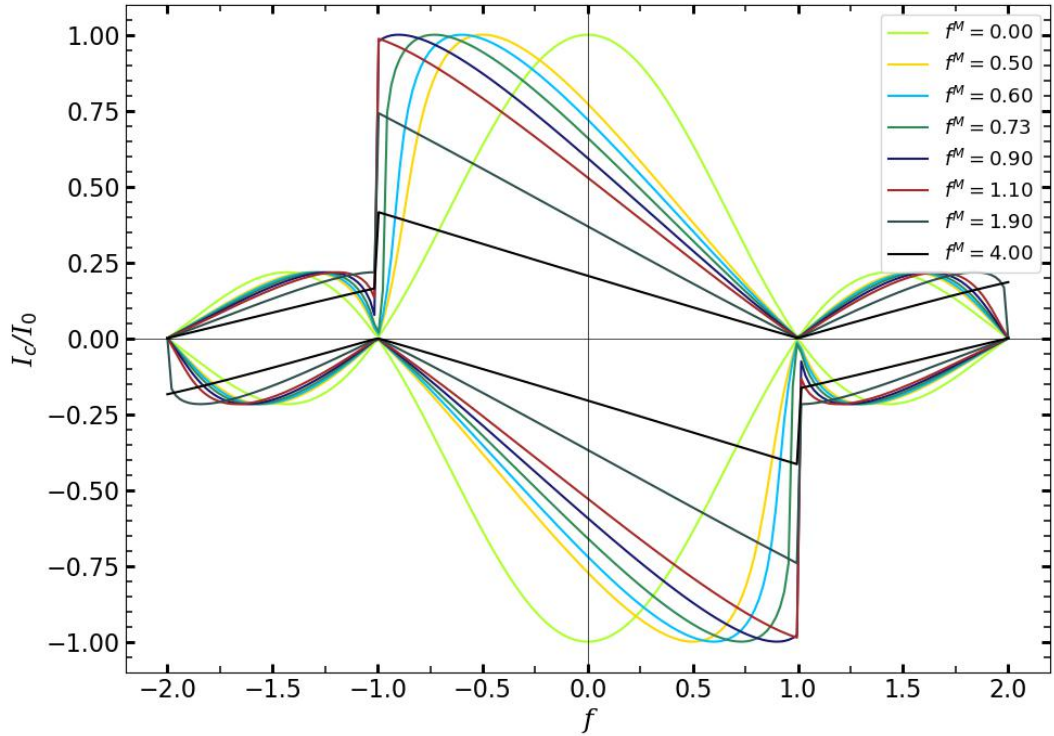
Figure 2.9: A family of asymmetric $I_c(f)$ for different f^M obtained by solving the eq. (2.5) numerically.

Note that the maximum asymmetry is achieved at the optimum point f_{opt}. Now let's examine the behavior of $\mathscr{A}$ as a function of f for different values of f^M. In Fig. 2.10(a), we can observe the dependence of the asymmetry parameter $\mathscr{A}$ on f for various fixed values of f^M. For instance, for the blue curve ($f^M = 0.6$), we find that the asymmetry parameter $\mathscr{A} \approx 8$ at the optimum value of $f_{\text{opt}} \approx -0.9$. This maximum asymmetry value increases as the value of f^M increases. In Fig. 2.10(b), we present the dependence of the maximum asymmetry $\mathscr{A}_{\text{max}}(f^M)$ at the optimum

value of f. One can see from both Fig. 2.10(a) and 2.10(b) that $\mathscr{A}$ increases with increasing f^{M}.
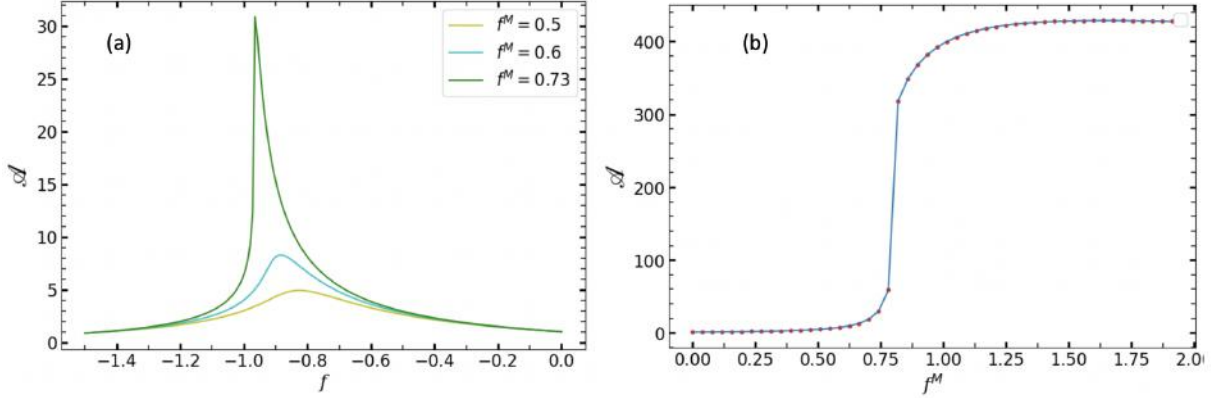
Figure 2.10: (a) Asymmetry parameter $\mathscr{A}$ vs. magnetic flux f for different values of f^{M}. (b) Maximum asymmetry parameter $\mathscr{A}$ vs. strength of in-line geometry f^{M}.

Thus, using in-line JJs and the appropriate applied normalized flux f, one is able to design a Josephson ratchet with a high asymmetry $\mathscr{A}$. It is important to emphasize that the maximum asymmetry achieved at f_{opt} for the curve with a high value of f^{M} exceeds 100, as shown in Fig. 2.10(b). At this f_{opt} one of the critical currents I_{c_+} vanishes while the other one I_{c_-} stays finite. Consequently, this leads to a divergence of the asymmetry parameter. However, it should be noted that achieving such high asymmetry in experiments is not feasible. In reality, the system is subjected to substantial amounts of noise affecting the amplitude of $|I_{\mathrm{c}_\pm}|$, especially near the optimal points, where one of the $|I_{\mathrm{c}_\pm}|$ should approach zero. This substantial noise leads to a substantial reduction in the actual asymmetry parameter compared to the theoretical value. Therefore, achieving extremely high asymmetry values as theoretically predicted is challenging in experimental settings.

In the next chapters, we will examine these challenges as well as the optimal target parameters for designing an effective Josephson ratchet. This will be done once we are prepared to commence the ratchet implementation.

Chapter 3

Fabrication and Implementation

3.1 Sample Information

The sample was prepared using a commercial YBCO thin film produced by a company named Ceraco. The detail information of the chip is provided by the company, as shown in Fig. 3.1(a). The sample was deposited layer-by-layer on a 2-inch LSAT substrate, starting with a buffer layer of cerium oxide (CeO), followed by a 30 nm $YBa_2Cu_3O_7$ (YBCO) film, and finally, a 20 nm layer of gold (Au) was deposited on top, as shown in Fig. 3.1(b).
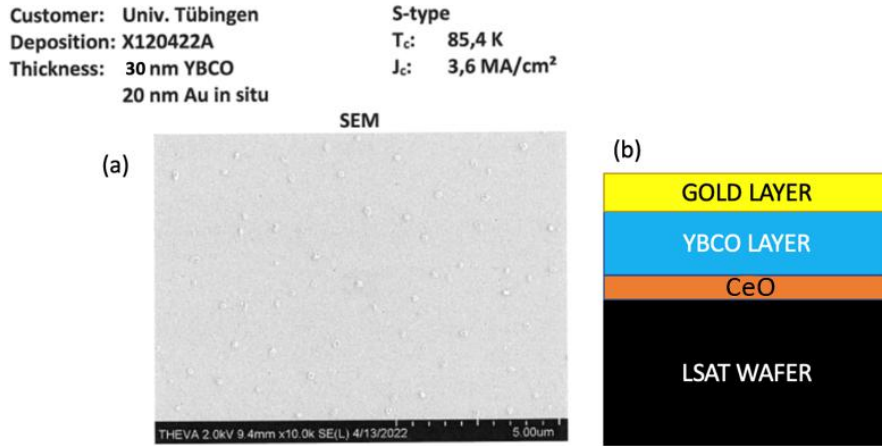
Figure 3.1: YBCO film on 2 inch LSAT substrate. (a) The scanning electron microscope picture of the sample surface. The critical temperature T_c and the value of the current density j_c are provided by Ceraco. (b) A schematic picture of the chip showing the deposited of layers.

3.2 Sample Layout

The general layout of a 5×5 mm^2 chip is shown in Fig. 3.2. It consists of two columns of 18 bridges, making a total of 36 bridges. Each bridge has two contact

pads on one side, and all the bridges are connected to the main central lines (vertical in Fig. 3.2), which is also connected to two ground pads on both sides.
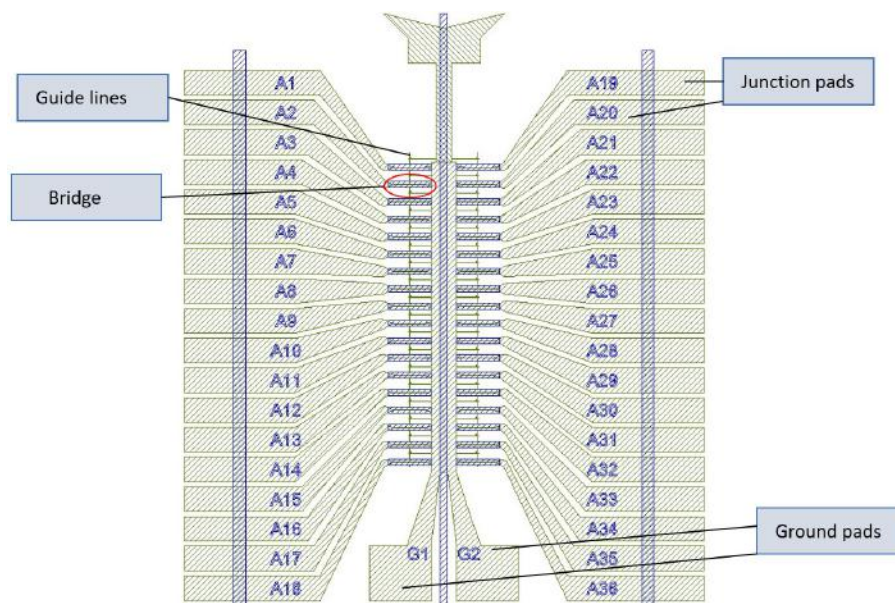
Figure 3.2: The layout of the sample. The hatched light green areas correspond YBCO covered by Au, while the blue areas represent Au removal mask down to YBCO. The guide lines are covered by Au. The Au layer is removed down to YBCO on the bridges, and along two vertical lines to provide separate pads for I & V contacts.

3.3 Sample Fabrication

The first step of the fabrication process involves dicing the 2 inches wafer with deposited films into 1×1 cm^2 chips. Each 1×1 cm^2 will be diced into four 5×5 mm^2 smaller chips with the layout shown in Fig. 3.2 after the etching steps.

The 1×1 cm^2 pieces are cleaned using an ultrasound bath filled with acetone, followed by two rounds of cleaning with isopropanol in an ultrasound bath. After dicing and cleaning, the sample is spin-coated with a photoresist called "ma-P1205" and later dried on a hotplate at 90° Celsius for 210 seconds. The chip is then placed into a maskless aligner for the patterning process, which consists of two steps.

(i). Etching of the gold: Once the chip is inside the maskless aligner, a laser beam scans the patterned layout shown in Fig. 3.3(a), which modifies the properties of the photoresist. The chip is then removed from the machine, and the modified photoresist is developed using "ma-D 331/S" for 50 seconds. It is quickly transferred to water to wash away the excess developer, and then transferred to another flask with water for further cleaning. The sample is then dried, and the gold is etched using an Argon ion beam. After the etching process is completed, the remaining photoresist is removed, and the chip is spin-coated again under the same mentioned conditions.

(ii). Etching of the YBCO: The chip is once again loaded into the maskless aligner to prepare with the second etching step. The same process as in step **(i)** is

carried out, but this time the machine scans another mask, as shown in Fig. 3.3(b) for a 1×1 cm^2 chip. The photoresist is modified again, and after removing the chip from the maskless aligner, it is selectively developed with "ma-D 331/S" and rinsed in water twice. Then, it is dried again, and the YBCO is etched with H$_3$PO$_4$ 0,1%. After the etching process, the remaining photoresist is removed once again, and the chip is ready to be diced once more. [10]

A 1×1 cm^2 chip is now divided into four similar smaller chips of 5×5 mm^2. Each small chip is labeled with a letter: A, B, C, and D. Each of them can accommodate 36 JJ. Zoom-in pictures of the bridges after each step of etching are shown in Fig. 3.4.
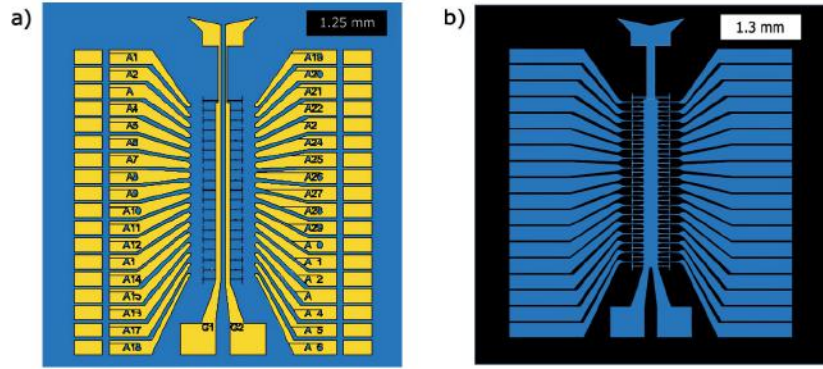
Figure 3.3: Masks used during the patterned process: (a) Mask used during step **(i)** for the etching of gold. The blue zone indicates where the gold has been removed, leaving only YBCO. The yellow zones indicate where the gold still remains. (b) The mask used during step **(ii)** for the etching of YBCO. The areas in blue represent the regions where the YBCO still remains. The black area represents LSAT (substrate). Note that in the regions where the gold remains from the first step (e.g., over the pads), it has not been removed during the second step.
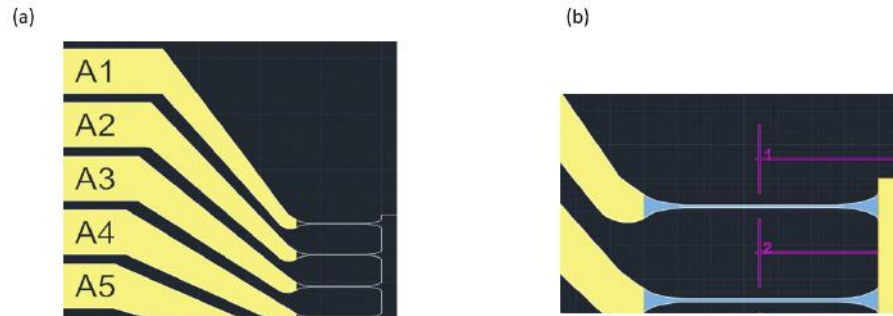
Figure 3.4: The microscope pictures of the sample after each step of the lithography process: (a) The pads after the step **(i)**. The dark areas represent YBCO, and the yellow areas represent Au. (b) the bridges after the step **(ii)**. The yellow area represents gold, the dark area represents LSAT, the blue area represents YBCO where the junctions will be finally irradiated, and the purple lines are guide lines for our next step using He-FIB.

We are now prepared to bring the sample to the Helium ion beam (He-FIB) laboratory in order to produce JJs and Josephson ratchets using the Focused Helium Ion Beam.

3.4   He-FIB

We utilize a He-FIB system with an energy of 30 keV to fabricate the Barrier Josephson junctions (BJJs). This is opposite to the JJs without a barrier, e.g., constriction-like JJs. The process is illustrated in Fig. 3.5, which provides a concise overview of the He-FIB technique.

The schematic illustration of producing BJJ using He-FIB is shown in Fig. 3.6. We create the Josephson barrier by irradiating the bridge along the line with a certain dose D (ions/nm). Dependence on the does D, the helium ions create either a very thin (few nm) amorphous region or a line (also a few nm wide) that suppresses T_c (changes doping in YBCO), thus acting as the barrier Josephson junction between two superconductors. In [11], it was experimentally shown that the critical current density j_c of the resulting BJJ depends on the irradiation dose D approximately as

$$j_c(D) \approx j_{c0} \exp(-D/D_0), \tag{3.1}$$

where j_{c0} is the critical current density at $D = 0$ and D_0 is the characteristic dose. They can be obtained by fitting the experimental data using eq. (3.1).

The BJJs made by He-FIB can be changed continuously from a conducting to a completely insulating state by varying the irradiation dose. In fact, high-dose He-FIB irradiation disturbs the internal atomic structure of YBCO, making the irradiated line amorphous and highly resistive. It can effectively act as a resistive wall with $j_c = 0$. We utilize this technique to fabricate Josephson ratchets with more complex geometries than BJJs (see, for example, Fig. 3.12).

3.5   Characterization

Before implementing the ratchet, we conducted a characterization of a series of BJJs with varying doses to determine the values of j_{c0} and D_0 for our specific chip. We fabricated 11 BJJs with dose series ranging between 450...700 ions/nm and subsequently measured the critical current of each junction. The results are presented Table. 3.1

Orion NanoFab - Helium Ion Microscope

Working Principle

The helium ions are produced at a tip of only three individual atoms, the trimer. Each of these atoms generates an ion beam in the helium atmosphere at the tip. The most intensive beam is selected and directed into the microscope's optics to reduce the beam diameter and to scan the focused beam sequentially in discrete locations in a raster x-y pattern on the specimen. At each discrete point, the interaction of the ion beam with the specimen produces secondary electrons. These secondary electrons are used for imaging as standard, whereby only SE from the top few nanometers of a surface contribute significantly to the signal.

Helium / Neon Ion Microscope

Technical Specifications

Scanning Ion microscope
Gas Field Ion Source (GFIS) with helium and neon
Field of view: 800 µm - 100 nm @ 8 mm working distance
Resolution: 0,35 nm @ He 30 kV 1,9 nm @ Ne 25 kV
Beam energy: He 10 - 30 kV; Ne 10 - 25 kV
Beam current: He 0,1 - 100 pA; Ne 0,1 - 50 pA
Everhart Thornley Secondary Electron Detector
Electron flood gun for charge compensation
Advanced Nanopatterning
Gas injection system with Pt-, W- or SiO_2-precurser
2 Kleindiek micromanipulators
Plasma cleaner

Gas Field Ion Source (GFIS)
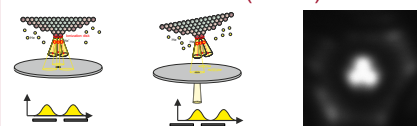
Typical performance metrics for a GFIS Gun
Operating extraction voltage:	25 - 35 kV
Operating Temperature:	60 - 90 Kelvins
Base Pressure:	< 4 x 10^{-10} Torr
Operating gas pressure:	1 x 10^{-7} - 5 x 10^{-6} Torr
Brightness:	5 x 10^{9} A m^{-2} sr^{-1}
deBroglie wavelength @30 kV:	~ 0.080 pm
Virtual source size:	< 0,25 nm
Total emitted current:	~ 150 pA

Substrate Interaction
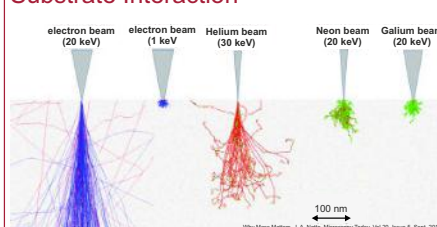
Simulations for 20 keV and 1 keV electron beams, a 30 keV helium beam, and 20 keV neon and gallium beams. The electron trajectories are shown in blue, and backscattered electrons are shown in red. The ion trajectories are shown in red, and the trajectories of recoiled sample atoms are shown in green. The simulated sample here is aluminum.

GFIS GUN / Ion Optical Column
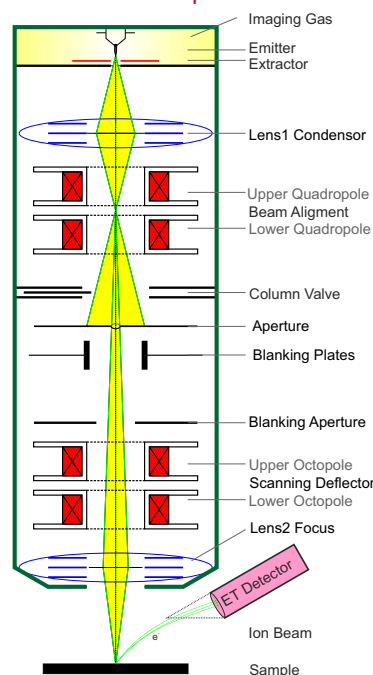
Figure 3.5: The poster about He-FIB.
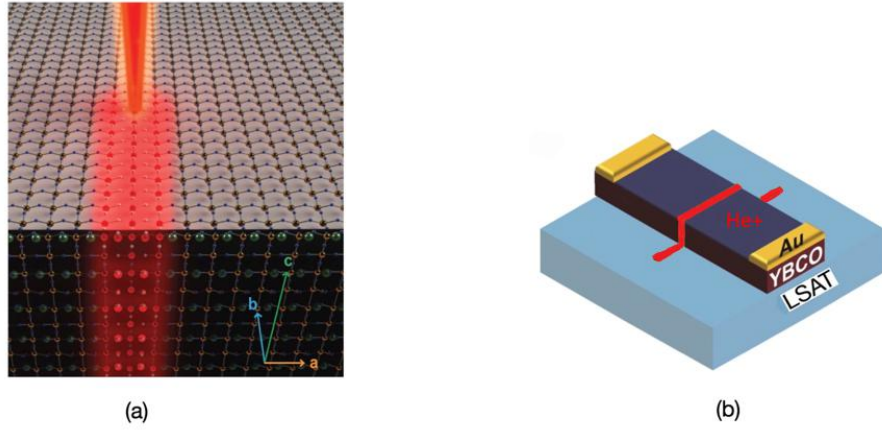
Figure 3.6: (a) The red line indicates focused He ion beam on the atomic level with a width of the order of a few nm. (b) Schematic sketch of the BJJ produced by He-FIB, where the red line indicates the barrier JJ.

BJJs	Dose (ions/nm)	Maximum I_c (µA)
D19	455	15.6
D20	455	13.2
D21	505	11.5
D22	505	6.8
D23	556	1
D24	556	3.7
D25	606	1.4
D26	606	0.59
D27	657	0.17
D28	657	0.79
D29	707	0.29

Table 3.1: The maximum I_c is determined by measuring $I_c(H)$ and selecting the highest value for each JJs.

Next, we wrote a short Python script to fit the experimental data using eq. (3.1) with j_{c0} and D_0 as fitting parameters. The result is shown in Fig. 3.7.
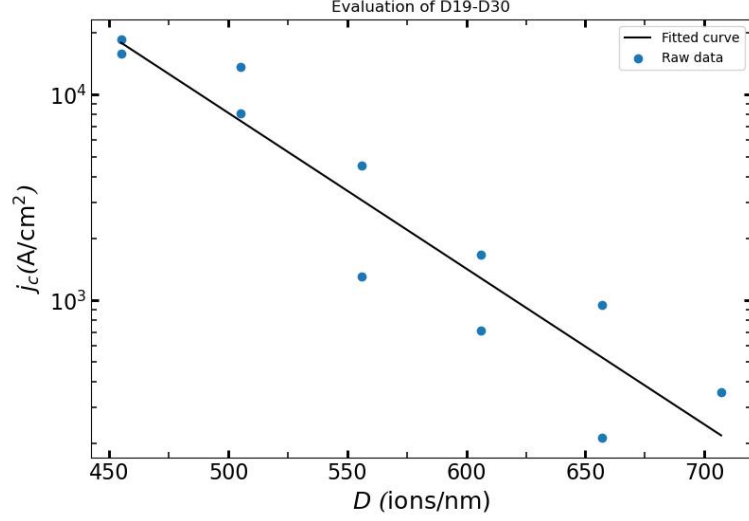
Figure 3.7: BJJs characterisation. Experimental measured $j_c(D)$ (symbols) and fit (line) using the eq. (3.1). In total, eleven BJJs measured with the $D \approx 450...700$ ions/nm. The width of the BJJs is $W = 2.8\,\mu m$.

As a result of fitting, we obtained $j_{c0} \approx 5 \times 10^7 A/cm^2$ and $D_0 = 57.2$ ions/nm. As an example, we present IVC and $I_c(H)$ of several BJJs in Fig. 3.8 to Fig. 3.11.
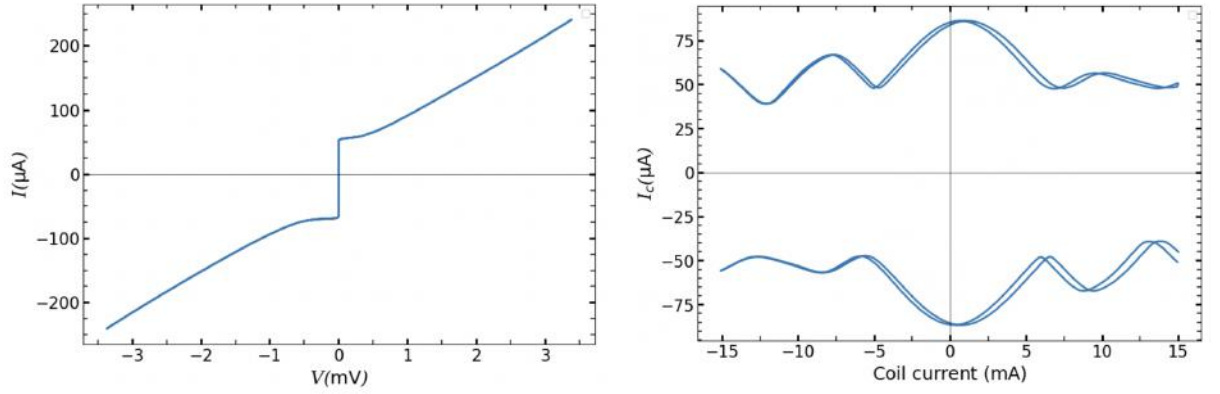
Figure 3.8: IVC and $I_c(H)$ of the junction B28 with $D = 350\,ions/nm$.
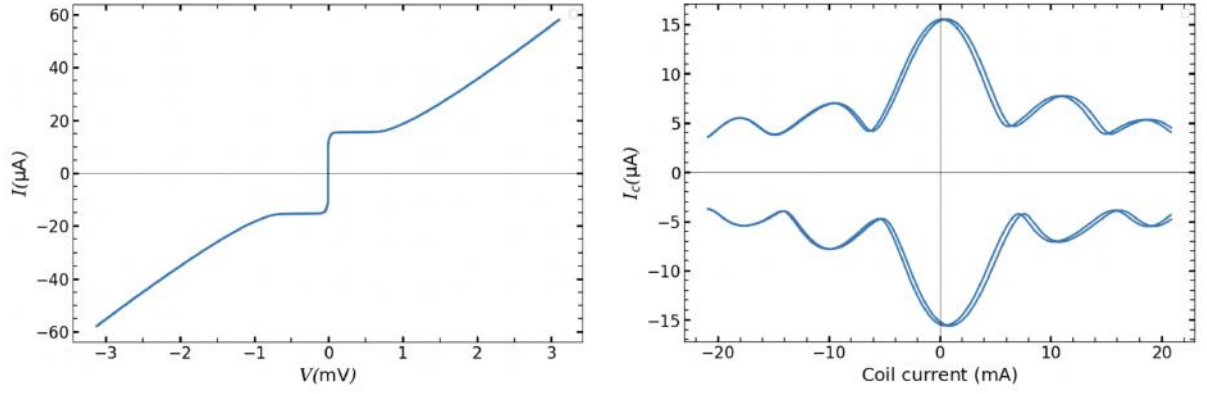
Figure 3.9: IVC and $I_c(H)$ of the junction D19 with $D = 450$ ions/nm.
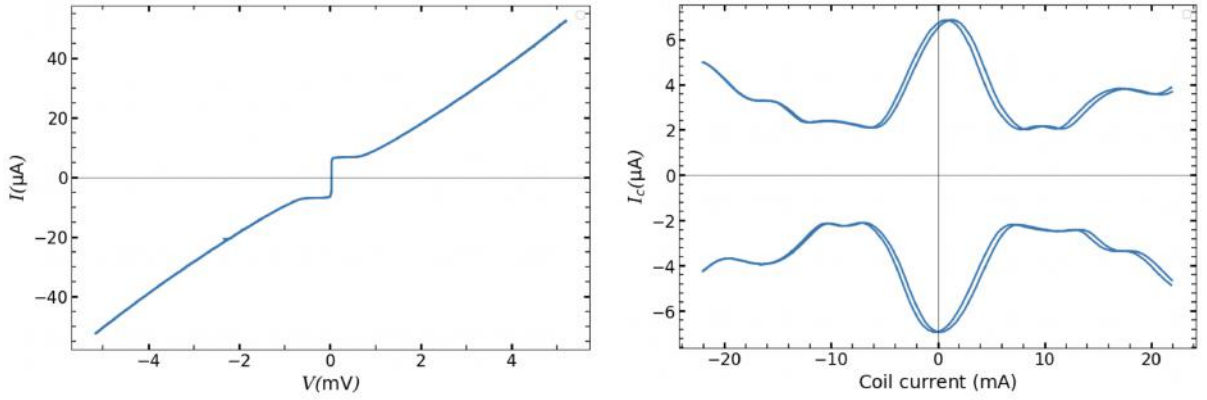
Figure 3.10: IVC and $I_c(H)$ of the junction D22 with $D = 505$ ions/nm.
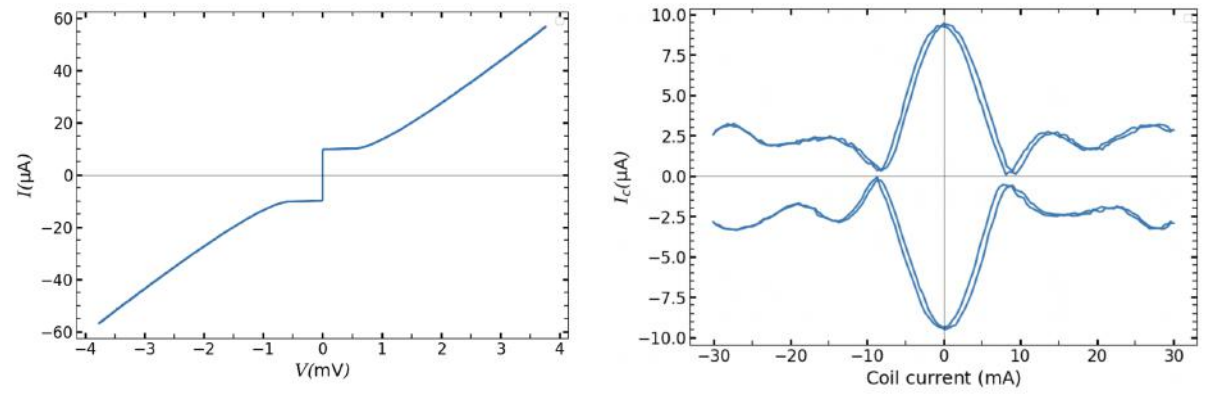
Figure 3.11: IVC and $I_c(H)$ of the junction B33 with $D = 600$ ions/nm.

3.6 Implementation of an In-line Geometry Josephson Ratchet

In the Chapter 2.1.3, we explored the impact of JJ of an in-line geometry on the generation of a self-field within our device. This field is characterized by f^{M}, which is described by the eq. (2.8). Additionally, we examined how this parameter influences the skewness of $I_{\mathrm{c}}(H)$ and, consequently, the asymmetry parameter.

In this master thesis, we focus on the implementation of a highly efficient ratchet based on reasonable theoretical parameters. For instance, eq. (2.8) clearly demonstrates the geometric dependences of the f^{M} on the length L and w. Therefore, we would design the ratchets with various values of f^{M}, while choosing the length L of the JJ through definition of f^{M} in eq. (2.8).

We propose to make a ratchet using the Josephson junction of an in-line geometry as presented in the Fig. 3.12, where the current flows to the junction from the side. To optimize the distance between the two resistive walls w, we must avoid making it too small (e.g., less than or equal to 100 nm) to prevent the destruction of the crystal configuration of YBCO due to the resistive walls. Analogously, extremely small values of w can lead to the emergence of topological defects. Throughout this work, we refrain from reducing w below 200 nm.
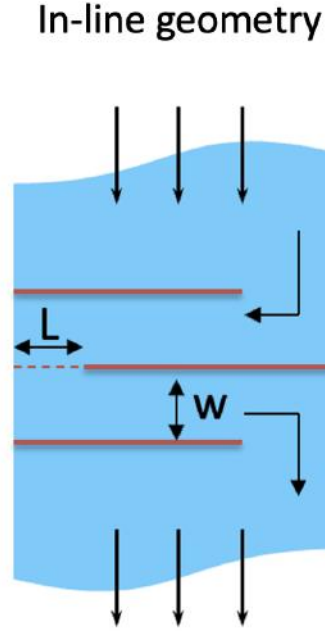
Figure 3.12: Sketch of the Josephson ratchet. The blue area is YBCO, the red solid lines are the resistive walls, dashed red line is the BJJ, and arrows indicate the flow of the supercurrent. w is the distance between two resistive walls and L is the length of the BJJ.

Hence, our target parameters are selected as follows: after choosing the desired value of the dimensionless parameter f^{M}, we choose the necessary supercurrent den-

sity $j_c(D)$ by adjusting the irridiation does D according to the eq. (3.1). From the value of j_c, we calculate the Josephson penetration depth λ_J and determine the appropriate length L using eq. (2.8). Knowing j_c we can find the critical current by $I_c = j_c \cdot L \cdot d$, where in our case, $d = 30\,\mathrm{nm}$.

It is important to mention that the expression for the Josephson penetration depth λ_J given by eq. (2.6) can be written to show the effect of the inductance of superconducting electrodes explicitly as

$$\lambda_J^K = \sqrt{\frac{\Phi_0 L}{2\pi j_c 2 L_K d}}, \tag{3.2}$$

where $L_K = \mu_0 \lambda^2 \dfrac{L}{w \cdot d}$ is the kinetic inductance. Substituting L_K into the eq. (3.2) gives us

$$\lambda_J^K = \sqrt{\frac{\Phi_0 w}{4\pi \mu_0 j_c \lambda^2}}. \tag{3.3}$$

Next, similar to the Chapter 2.1.3, we can write f_K^M with respect to the λ_J^K as

$$f_K^M = \frac{5 L^3 d_{\mathrm{eff}}}{24\pi (\lambda_J^K)^2 w d'}, \tag{3.4}$$

where $d' = 2\lambda \coth(w/\lambda)$.

In Table. 3.2, we present two sets of target parameters for the ratchets A15 and A22, which will be discussed in detail later.

Target Parameters	A15	A22
$w(\mathrm{nm})$	300	200
$D(\mathrm{ions/nm})$	507	531
$j_c\ (\mathrm{kA/cm^2})$	7.15	4.8
$I_c(\mu\mathrm{A})$	3.8	2.5
$\lambda_J(\mathrm{nm})$	250	250
$L(\mathrm{nm})$	1750	1750
$l \equiv L/\lambda_J$	7	7
f^M	0.25	0.26
$\lambda_J^K(\mathrm{nm})$	2960	2960
$l_K \equiv L/\lambda_J^K$	0.6	0.6
f_K^M	0.09	0.1

Table 3.2: Comparison of target parameters between ratchet A15 and A22.

Chapter 4

Experimental Results

4.1 An Overview

In this chapter, we report a set of experimental results for the ratchets A22 and A15. First, we compare the actual (experimental) and target (theoretical) parameters of each devices. Then we present our experimental data, including IVC, $I_\text{c}(H)$, $\overline{V}_\text{dc}$, $\overline{P}_\text{out}$, $\overline{P}_\text{in}$, and, finally, the efficiency η. Afterward, we compare our experimental results with their simulations in the quasistatic regime. Finally, we drive our system with stochastic drive and investigate the effect of different types of noises, such as external and internal noises plus possibly some other sources. It is shown that internal noise can be rectified into the output dc voltage.

4.2 Josephson Ratchet A22

In Table. 4.1, the target and parameters of the device A22 are presented.

A22	Target parameter	Actual parameter
$w(\text{nm})$	200	200
$D(\text{ions/nm})$	531	531
$j_\text{c}\ (\text{kA/cm}^2)$	4.8	28
$I_\text{c}(\mu\text{A})$	2.5	14.8
$\lambda_\text{J}(\text{nm})$	250	103
$L(\text{nm})$	1750	1750
$l_j \equiv L/\lambda_\text{J}$	7	17
f^M	0.26	1.54
$\lambda_\text{J}^\text{K}(\text{nm})$	2960	1220
$l_K \equiv L/\lambda_\text{J}^\text{K}$	0.6	1.4
f_K^M	0.1	0.63

Table 4.1: Comparison of target and actual parameters of ratchet A22. Notice that we assumed $\lambda = 250\,\text{nm}$ and subsequently $\lambda_\text{eff} = 2\,\mu\text{m}$.

In general, discrepancies between the actual and the target parameters can arise due to various factors such as fabrication techniques (lithography processes), and the accuracy of I_c measurements. The dose D has a high precision of around two percent.

Since the positionary precision of He-FIB is ~ 1 nm, our geometric parameters, such as length L and w, are also quite accurate. According to eq. (3.1), the value of j_c has an exponential dependence on the dose, so that the spread is quite high, which is typical for our technology. Consequently, I_c, λ_J, the normalized length l_j, and f^M follow their definitions and depend on the actual j_c value.

Since we are working in the thin film limit, where $d \ll \lambda$, our $\lambda_{\text{eff}} = \dfrac{\lambda^2}{d} = 2\,\mu\text{m}$, as we defined in the section. 2.1.3. In this limit, the contribution of kinetic inductance becomes dominant. Therefore, we use kinetic inductance in the definition of the Josephson penetration depth (see eq. (3.3)) to get $\lambda_J^K = 2.9\,\mu\text{m}$, which is comparable to λ_{eff}. In this case, the phase $\varphi(t, \mathbf{x})$ in our JJ is described by the non-local model [12]. To our knowledge, the dependence of $I_c(B)$ in the in-line geometry for non-local JJ has not been found in the literature, and its dependence on the parameters, in particular the asymmetry, is unknown. Therefore, we use the parameters for the local models (see target parameters in Table. 4.1) as a rough estimate, and iteratively investigate many JJ parameters to arrive to a high value of asymmetry.
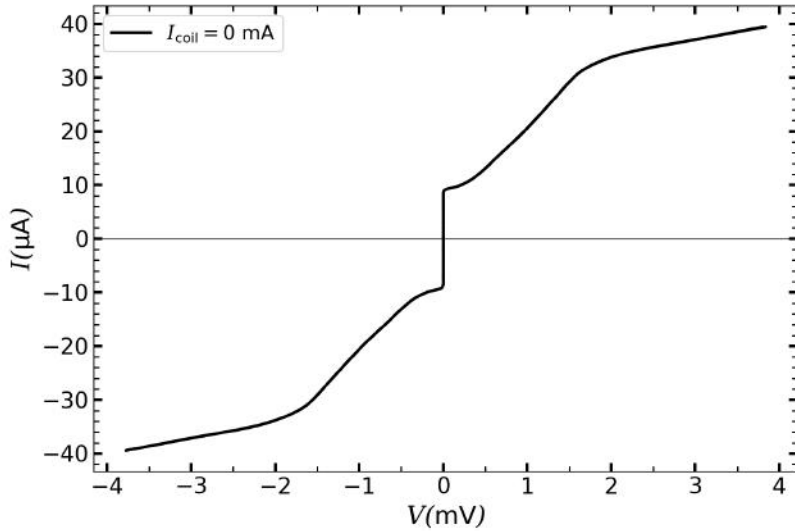
Figure 4.1: IVC of the ratchet A22 at $I_{\text{coil}} = 0$ where $|I_{c_+}| \approx |I_{c_-}| \approx 8.43\,\mu\text{A}$.

The IVC of the ratchet A22 is presented in Fig. 4.1. The normal resistance $R_N \approx 50\,\Omega$. It is roughly determined by the slope at a current of $I \approx 30\,\mu\text{A}$, where the voltage is $V \approx 1.5\,\text{mV}$. It is worth noting that the observed bending near $|I| \approx \pm 32\,\mu\text{A}$ may be due to the small distance w between the two resistive walls. As a result, there is a possibility of some YBCO crystal destruction between RWs, creating a quasi-junction in series with the JJ of the ratchet. This leads to a bending of the

IVC around $|I| \approx \pm 32\,\mu\text{A}$. However, the exact cause cannot be determined with the absolute certainty.
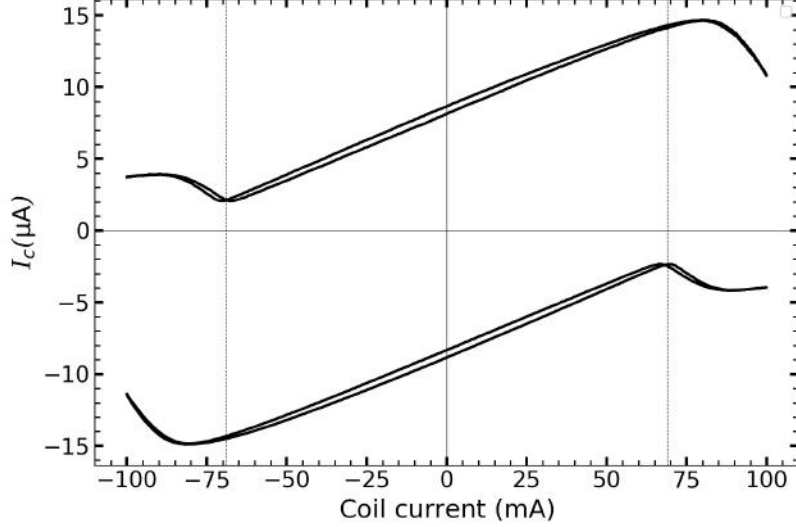
Figure 4.2: Critical current versus magnetic coil current of the Josephson ratchet A22. We used a voltage criterion equal to $1\,\mu\text{V}$ for this measurement.

The dependence of $I_{c_\pm}(I_{\text{coil}})$ is shown in Fig. 4.2. The coil current I_{coil} generates a magnetic field B perpendicular to the sample plane. The coil factor we used for our measurement is approximately $0.17\,\text{mT/A}$. Within our coil-current range of ± 100 mA, we can clearly observe the skewed nature of $I_c(I_{\text{coil}})$. Using Fig. 4.2, we can identify the optimal magnetic field, at which the asymmetry parameter $\mathscr{A}$ reaches its maximum. To observe the dependence of asymmetry parameter (see eq. (2.1)) on I_{coil}, we have plotted $\mathscr{A}(I_{\text{coil}})$ as shown in Fig. 4.3.
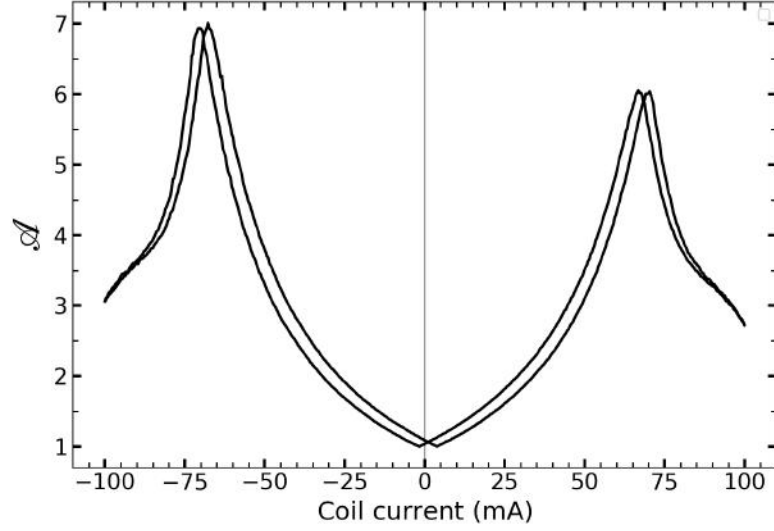
Figure 4.3: The dependence of the value of the asymmetry parameter $\mathscr{A}$ on I_{coil}. The maximum asymmetry $\mathscr{A} \approx 7$ is at $I_{\mathrm{coil}} \approx -69\,\mathrm{mA}$.

We observe that $\mathscr{A}$ is somewhat asymmetric with respect to the polarity of I_{coil}. For instance, $\mathscr{A}(69\,\mathrm{mA}) \approx 6$, whereas $\mathscr{A}(-69\,\mathrm{mA}) \approx 7$. This asymmetry can be attributed to several factors, such as the shift of zero of the current source used to bias the JJ or the design of our ratchet itself.

Another issue is the discrepancy between the theoretically predicted $\mathscr{A}$ and its experimental value. As briefly mentioned on page. 23, this difference is mainly due to finite voltage noise, which led us to choose a voltage criterion. This results in the background I_{c} value[1]. Therefore, the measured $I_{\mathrm{c_+}}$ can never reach any value below this background value. This prevents the value of $I_{\mathrm{c_+}}$ from approaching zero at the optimum point, as presented theoretically in section. 2.1.3. Thus, the maximum value of asymmetry given by eq. (2.1) is effectively limited. Another possible reason for such a difference is that, e.g., our experimental I_{c}, see Fig. 4.2, looks qualitatively different from theoretical one in Fig. 2.9. For example, the minimum and maximum of $I_{\mathrm{c_\pm}}$ in Fig. 2.9 for $f^{\mathrm{M}} > 0.9$ correspond to the same value of coil current, however in the experiment they are not. Therefore, one can expect such a differences of $\mathscr{A}$ in the theory and the experiments.

Anyway, the main goal for us is to find the optimum I_{coil} where $\mathscr{A}$ has a maximum. Once we have determined the optimum magnetic field, we apply it to our device and measure the IVC, as shown in Fig. 4.4.

---

[1]The background I_{c} value is defined by $I_{\mathrm{c}}^{\mathrm{Background}} = V_{\mathrm{criterion}}/R$.
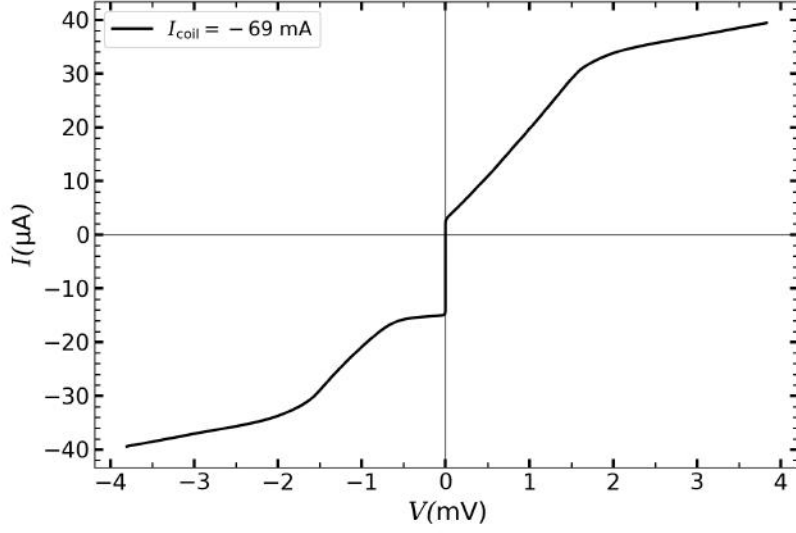
Figure 4.4: The asymmetric IVC of the ratchet A22 at the optimum magnetic field (coil current) $I_{\text{coil}} = -69\,\text{mA}$ exhibits $|I_{c_+}| \approx 1.53\,\mu\text{A}$ and $|I_{c_-}| \approx -13.8\,\mu\text{A}$, resulting in $\mathscr{A} \approx 7$.

Having such an asymmetric IVC, we can now apply an ac-drive, which is defined by

$$I(t) = I_{\text{ac}}\sin\omega t, \tag{4.1}$$

and measure the rectification curve $\overline{V}_{\text{dc}}(I_{\text{ac}})$, as shown in Fig. 4.5.
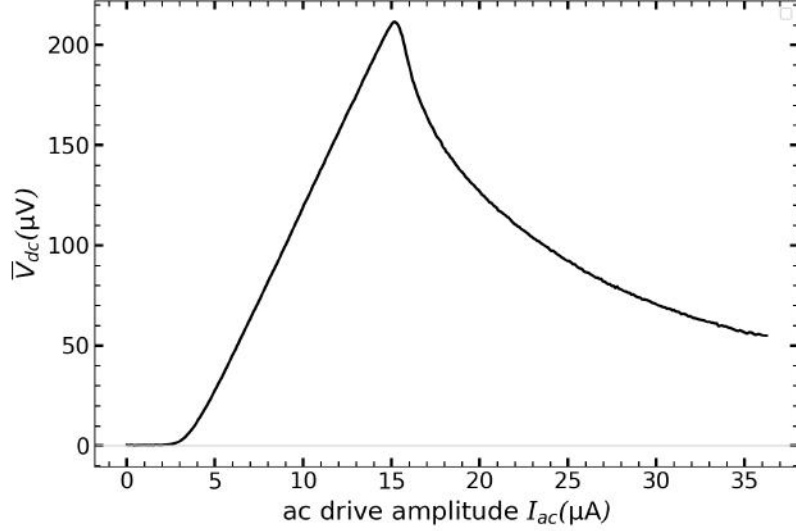
Figure 4.5: The rectification curve for the ratchet A22 at $I_{\text{coil}} = -69\,\text{mA}$, where $|I_{c_-}| \approx 15.2\,\mu\text{A}$, $|I_{c_+}| \approx 2.2\,\mu\text{A}$ and RW $\Delta \approx 13\,\mu\text{A}$.

To do this, for each value of I_{ac}, the rectified voltage is experimentally measured over 5 ms, which corresponds to one period of the drive.[2] This curve is shown in Fig. 4.5. One can explain the behaviour of $\overline{V}_{dc}(I_{ac})$ using the asymmetric IVC (see Fig. 4.4) as follows. For a small amplitude of ac-drive $I_{ac} < |I_{c_+}|$, $V(t)$ remains zero, so $\overline{V}_{dc}$ remains zero too in Fig. 4.5. When the ac-drive amplitude exceeds $|I_{c_+}| \approx 2.2\,\mu$A, the voltage becomes positive $V(t) > 0$ during some part of the positive semi-period of ac-drive in Fig. 4.4. This leads $\overline{V}_{dc} > 0$ in Fig. 4.5. By increasing the amplitude of ac-drive further, the rectified $\overline{V}_{dc}$ reaches its maximum $\overline{V}_{dc} \approx 215\,\mu$V at $I_{ac} \to |I_{c_-}| \approx 15.2\,\mu$A. If ac-drive amplitude is increased further ($I_{ac} > |I_{c_-}|$), $V(t)$ becomes negative (instead of zero) during the negative semi-period of ac-drive. Thus, the net average voltage decreases and approaches zero in the limit of large I_{ac}.

At this stage our ratchet is idle. To load it, we apply some counterforce I_{dc} in the opposite direction of the particle motion. This force effectively tilts the potential and, because of the ratchet effect, the particle will climb uphill and generate some useful work. The rectification curves, illustrating the operation of loaded ratchet for different values of I_{dc}, are shown in Fig. 4.6.
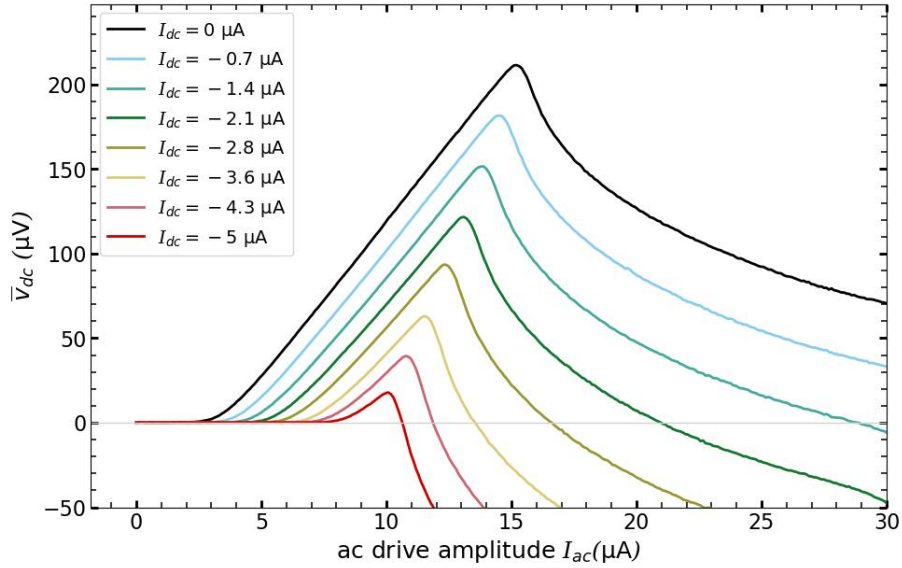
Figure 4.6: The rectification curve for the ratchet A22 at $I_{coil} = -69\,$mA for several I_{dc} from 0 (idle ratchet) up to $|I_{dc}| = 5\,\mu$A.

We observe that as the absolute value of the counterforce increases, the RW gradually decreases until it eventually closes at the stopping force of $|I_{dc}| = |I_{stop}| \approx 5.5\,\mu$A. The value of stopping force I_{stop} is given by [4]

$$I_{stop} = \frac{|I_{c_-}| - |I_{c_+}|}{2},$$

---

[2]For our measurement setup, we employed 500 samples per period and $f = \omega/2\pi = 200\,$Hz, and so sampling rate equals to 100 k samples/sec.

which for our Josephson ratchet A22 $|I_{\text{stop}}| \approx 6.1\,\mu\text{A}$. It closely coincides with our experimental finding of around $|I_{\text{stop}}| \approx 5.5\,\mu\text{A}$.

Now we can measure the output and input power, and estimate the efficiency in different regions.

To calculate the output power $\overline{P}_{\text{out}}$, we multiply $\overline{V}_{\text{dc}}(I_{\text{ac}})$ with the corresponding values of I_{dc} as

$$\overline{P}_{\text{out}}(I_{\text{ac}}) = \langle V \cdot I_{\text{dc}} \rangle = \overline{V}_{\text{dc}}(I_{\text{ac}}) \cdot I_{\text{dc}}, \tag{4.2}$$

and calculate the output power. The result is presented in Fig. 4.7(a). We observe that increasing I_{dc} leads to an increase in $\overline{P}_{\text{out}}$ until $I_{\text{dc}} = -2.8\,\mu\text{A}$. Further increases in I_{dc} cause a decrease in $\overline{P}_{\text{out}}$ as can be also understood using eq. (4.2): at high I_{dc} average voltage $\overline{V}_{\text{dc}}$ decreases and tends to zero (or even to negative values) for $I_{\text{dc}} > |I_{\text{stop}}|$.

Then we also measure the input power $\overline{P}_{\text{in}} = \langle V(I(t)) \cdot I(t) \rangle$. Measuring $\overline{P}_{\text{in}}$ presents a challenging situation as we were unable to extract $I(t)$ from the average or integral, similar to what we did with I_{dc} for $\overline{P}_{\text{out}}$. To overcome this challenge, we manually performed measurements for six I_{ac} values chosen from the curves in Fig. 4.6. For each value, we measured $V(t)$ and multiplied it by $I(t)$, followed by integration. The expression for calculating $\overline{P}_{\text{in}}(I_{\text{ac}})$ is given by

$$\overline{P}_{\text{in}}(I_{\text{ac}}) = \frac{1}{T} \int_0^T V(t) \cdot I(t) dt.$$

The results are plotted in Fig. 4.7(b).

Finally, we calculate the efficiency as shown in Fig. 4.7(c). We observe that unlike $\overline{P}_{\text{out}}$, the efficiency constantly increases as the value of $|I_{\text{dc}}|$ increases, while the RW decreases. Furthermore, for every value of I_{dc}, the maximum efficiency occurs at the beginning of the RWs, which is in accordance with the predictions and simulations presented in Chapter 2.
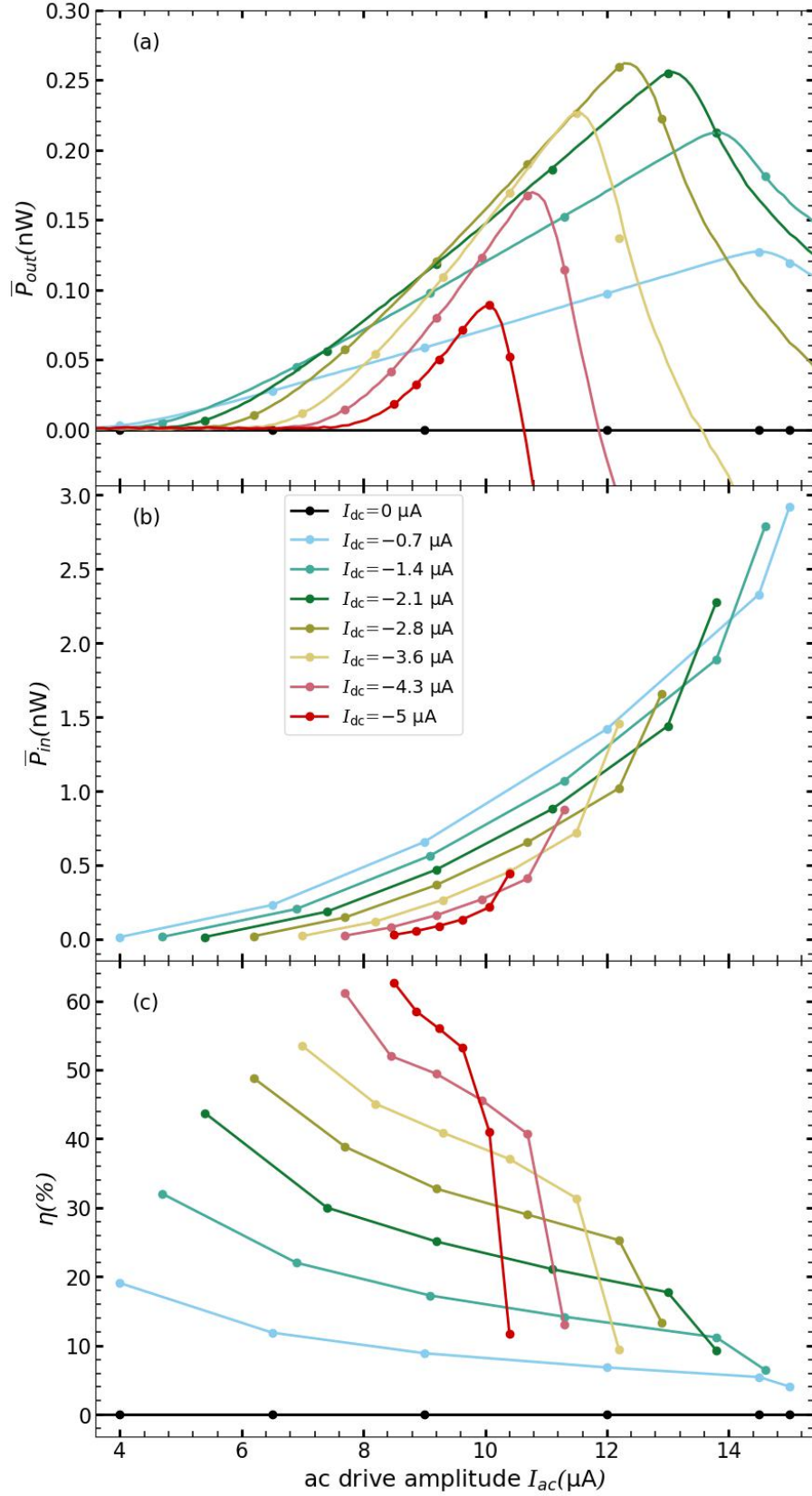
Figure 4.7: Experimental data for (a) $\overline{P}_{\text{out}}(I_{\text{ac}})$, (b) $\overline{P}_{\text{in}}(I_{\text{ac}})$, and (c) efficiency $\eta(I_{\text{ac}})$ for the ratchet A22.

4.2.1 Numerical Calculations of Ratchet A22 characteristics

In the quasistatic regime, the behaviour of the system is fully defined by the experimental IVC. Therefore, starting from the experimental IVC, one can obtain all the characteristics such as $\overline{V}_{dc}, \overline{P}_{out}$ and $\overline{P}_{in}$ for different I_{dc} and extract the figures of merit. To numerically obtain $\overline{V}_{dc}(I_{ac})$, we measure a high-resolution experimental asymmetric IVC, interpolate it, and then numerically calculate

$$\overline{V}_{dc}(I_{ac}) = \frac{1}{T} \int_0^T V\Big(I(t) + I_{dc}\Big) dt,$$

for the loaded ratchet. The result is plotted in Fig. 4.8.

Next, we perform the similar calculations to obtain $\overline{P}_{in}$, $\overline{P}_{out}$, and finally η, see Fig. 4.9. Simultaneously, all numerically obtained plots are compared with their corresponding experimental data from Fig. 4.7.

Figure 4.8: Numerically calculated $\overline{V}_{dc}(I_{ac})$ (lines) and the corresponding experimental data (dots) from Fig. 4.6 for the ratchet A22.

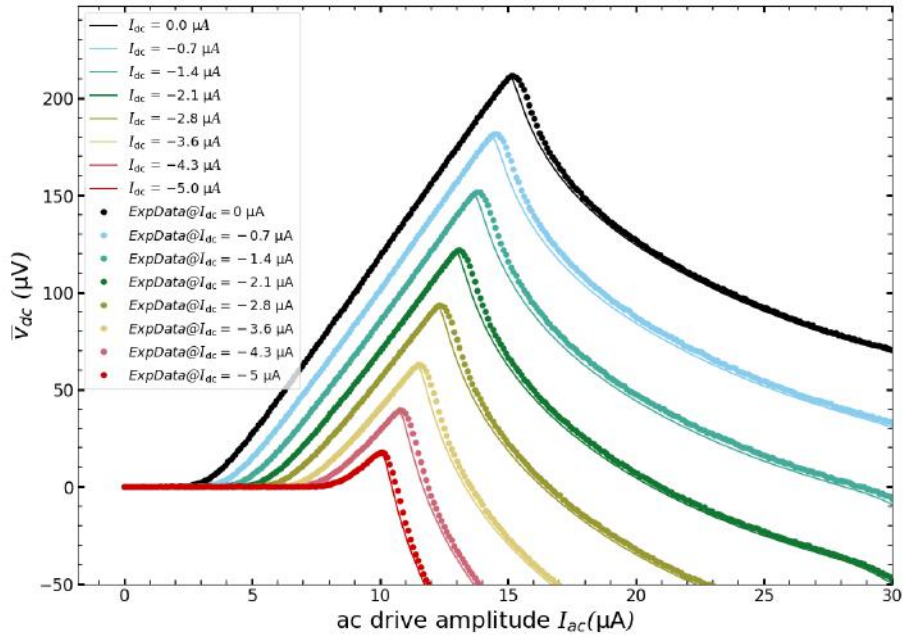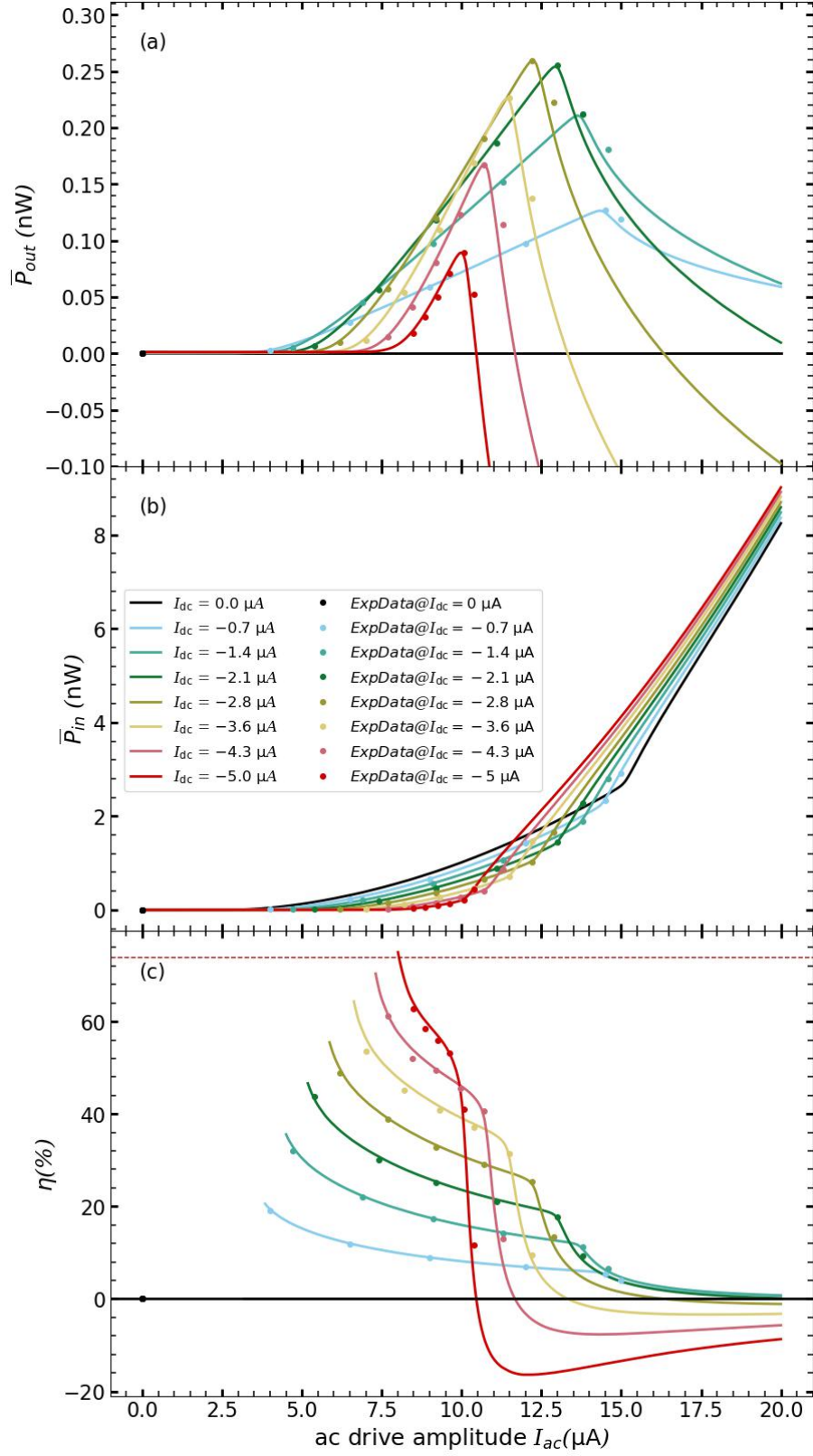Figure 4.9: Numerical obtained curves (lines) versus the experimental data (dots) for (a) $\overline{P}_{\text{out}}(I_{\text{ac}})$. (b) $\overline{P}_{\text{in}}(I_{\text{ac}})$. (c) $\eta(I_{\text{ac}})$ for the ratchet A22.

One important observation is that, for $I_{ac} < 2...3\mu A$, the powers approach zero, resulting in the efficiency tending towards 0/0 with large uncertainty. To address this issue, we impose a cut-off criterion of $P_{in} \leq 10\,\mathrm{pW}$ and do not calculate the efficiency below this cut-off.

We see that our directly measured experimental data coincide well with our numerical results based on the experimental IVC. It is enlightening to mention that the theoretical maximum efficiency calculated in [4] (red dashed line in Fig. 4.9(c)) is around 74%, which nicely touches our maximum numerical calculated $\eta(I_{ac})$ curve (the red curve in Fig. 4.9(c)) at I_{dc} around stopping current. In Table. 4.3, we compare our Josephson ratchets with other Josephson ratchet reported in the literature.

4.3 Josephson Ratchet A15

In this section, we will present the experimental results for ratchet A15, similar to the previous section. A comparison between the actual and target parameters is provided in Table 4.2.

A15	Target parameter	Actual parameter
$w(\mathrm{nm})$	300	300
$D(\mathrm{ions/nm})$	507	507
$j_c\ (\mathrm{kA/cm^2})$	7.1	53
$I_c(\mu A)$	3.7	28
$\lambda_J(\mathrm{nm})$	250	129
$L(\mathrm{nm})$	1750	1750
$l_j \equiv L/\lambda_J$	4.9	13.5
f^M	0.25	0.96
$\lambda_J^K(\mathrm{nm})$	2960	1090
$l_K \equiv L/\lambda_J^K$	0.6	1.6
f_K^M	0.09	0.6

Table 4.2: Comparison table of target and actual parameters of ratchet A15.

The IVC of ratchet A15 is shown in Fig. 4.10
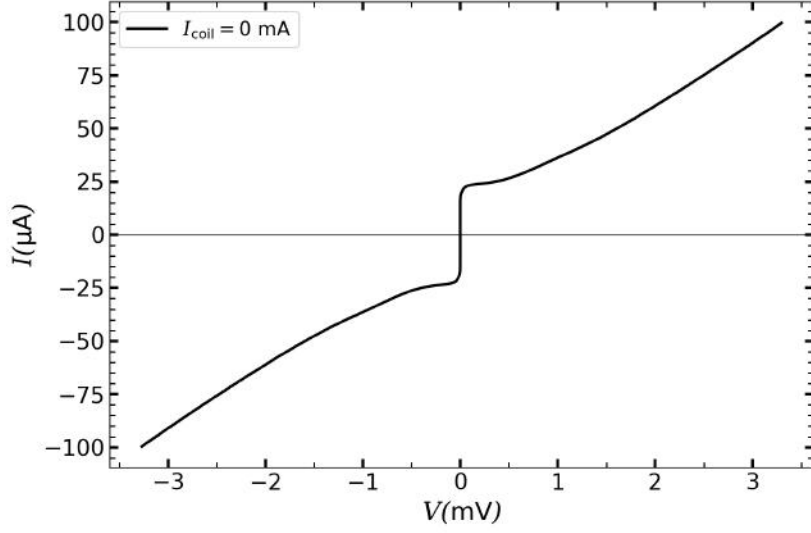
Figure 4.10: IVC of the ratchet A15 at $I_{\text{coil}} = 0$. $|I_{c_+}| = |I_{c_-}| \approx 21\,\mu\text{A}$ and $R_N \approx 32\,\Omega$.

As we can see, there is no bending in the IVC as seen in Fig. 4.1 because for the ratchet A15, we chose $w = 300\,\text{nm}$; therefore, there is no crystal destruction of YBCO due to the distance between the resistive walls. All the other experimental results for this ratchet, similar to the Josephson ratchet A22, are presented in Figs. 4.11 to 4.16.
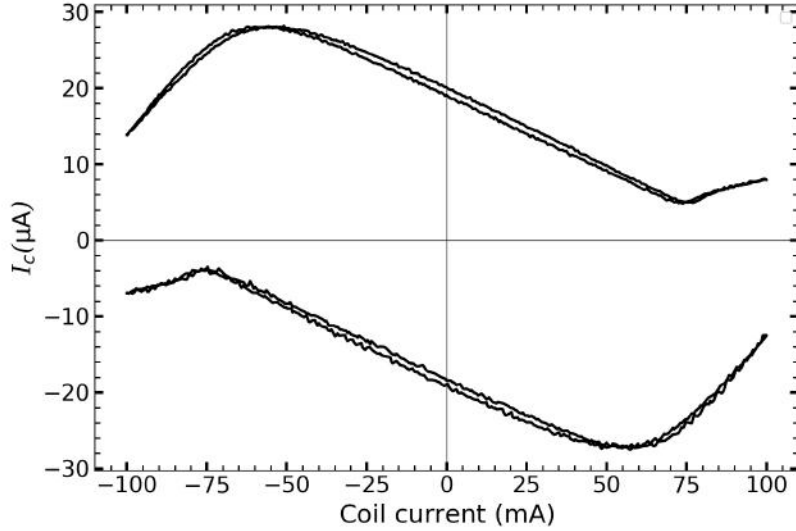
Figure 4.11: Critical current versus magnetic coil current of the ratchet A15.
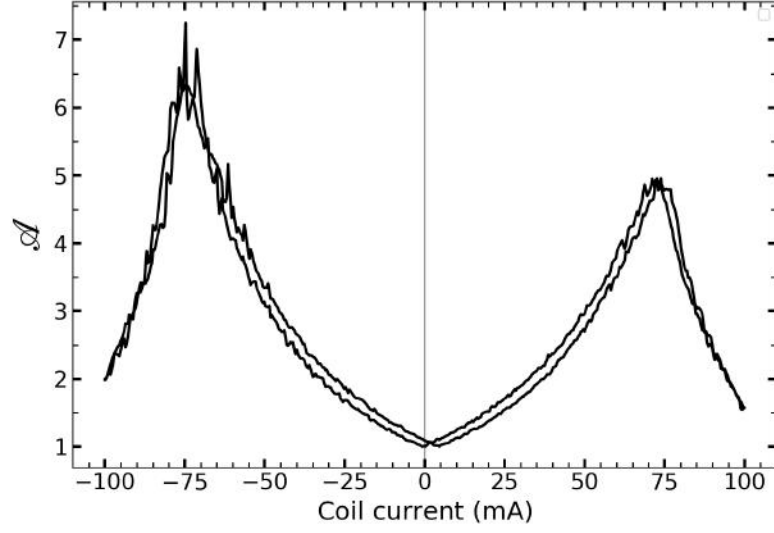
Figure 4.12: The value of asymmetry parameter, which shows the maximum asymmetry $\mathscr{A} \approx 7$ at optimum magnetic $I_{\text{coil}} = 75\,\text{mA}$.
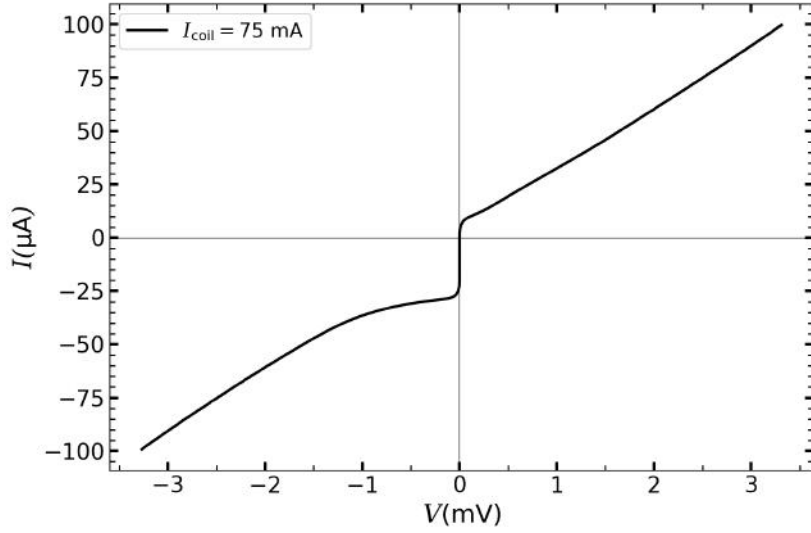
Figure 4.13: An asymmetric IVC of the ratchet A15 at the optimum $I_{\text{coil}} = 75\,\text{mA}$ has $|I_{\text{c}_-}| \approx 24.5\,\text{µA}$ and $|I_{\text{c}_+}| \approx 3.5\,\text{µA}$.
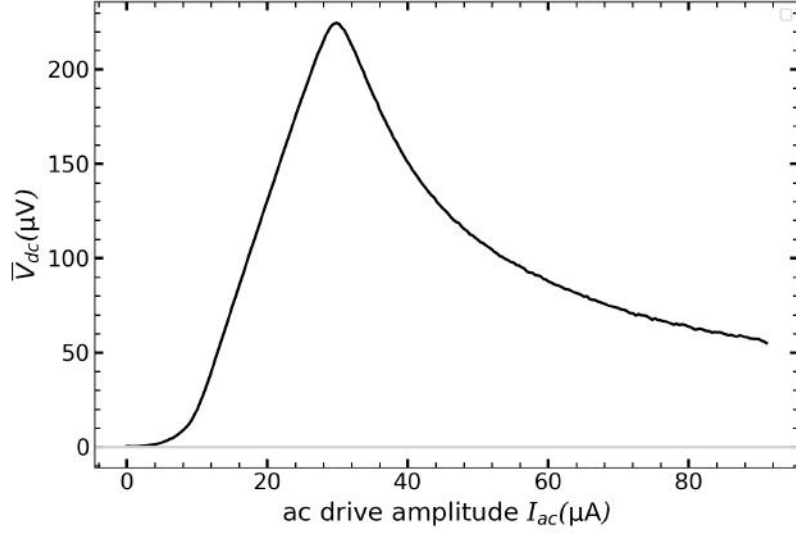
Figure 4.14: The rectification curve $\overline{V}_{\mathrm{dc}}(I_{\mathrm{ac}})$ for the ratchet A15 at $I_{\mathrm{coil}} = 75\,\mathrm{mA}$ with maximum dc average voltage $\overline{V}_{\mathrm{dc}}(I_{\mathrm{ac}}) \approx 225\,\mathrm{V}$.
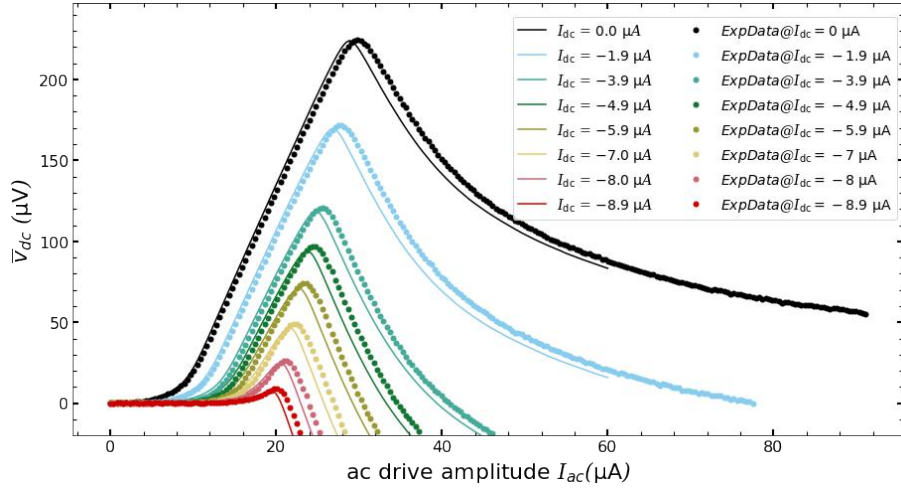
Figure 4.15: Numerical obtained curves (lines) versus the experimental data (dots) of $\overline{V}_{\mathrm{dc}}(I_{\mathrm{ac}})$ for the loaded ratchet A15 at $I_{\mathrm{coil}} = 75\,\mathrm{mA}$ for several I_{dc} up to stopping force $|I_{\mathrm{dc}}| = 8.92\,\mathrm{\mu A}$.
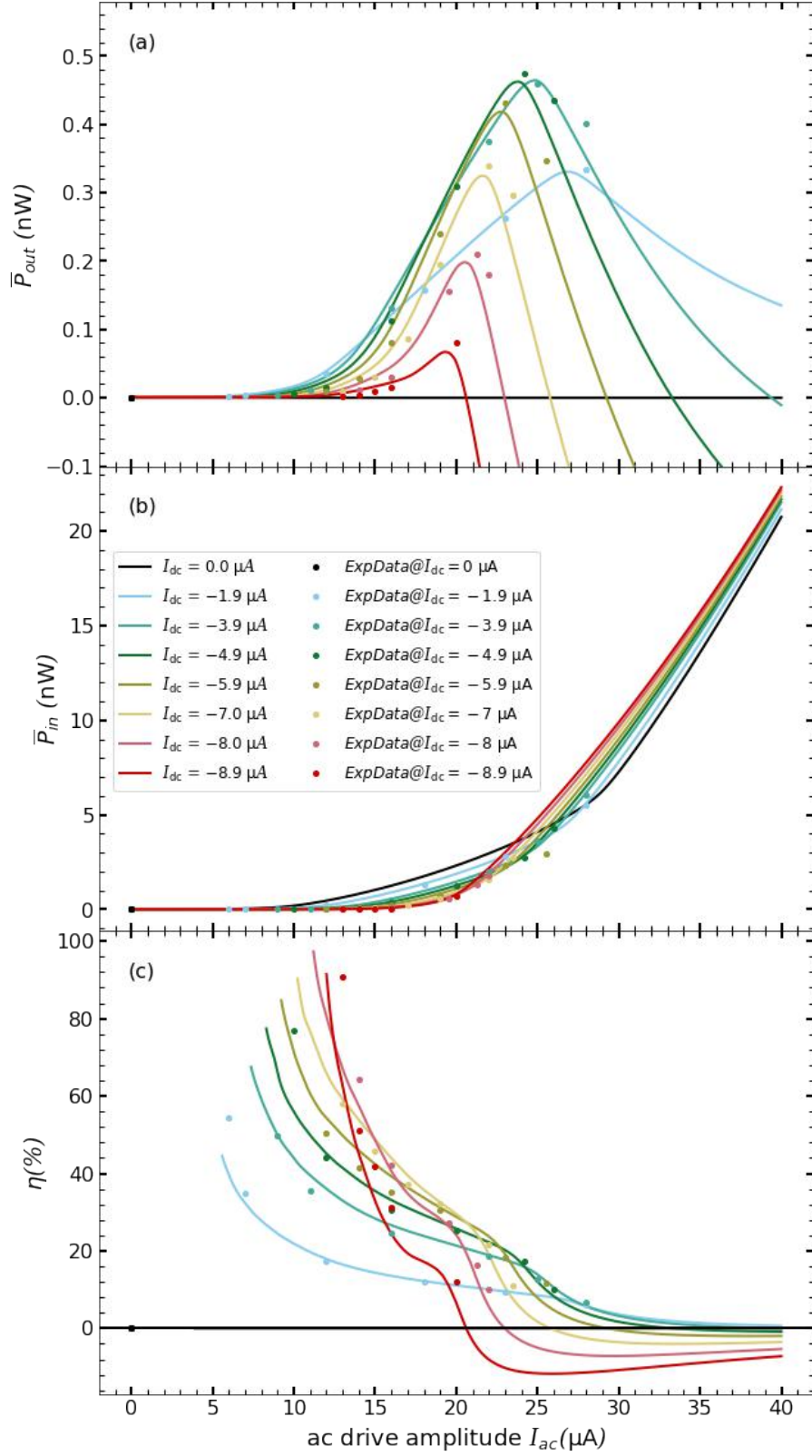
Figure 4.16: Numerical obtained curves (lines) versus the experimental data (dots) of (a) $\overline{P}_\text{out}$, (b) $\overline{P}_\text{in}$, and (c) Efficiency η for the ratchet A15.

4.4 Driving the Ratchet with a Stochastic Signal

In this section, our objective is to examine the influence of different types of noise on the system and assess their impact. Usually noise is considered as a negative effect onto the system because it disturbs the system and, e.g., diminishes the measurement accuracy. On the other hand, one can use these noises as a source of energy and rectify it. In this thesis, we explore two distinct types of noise: external and internal noises.

To generate external noise, we consider random normal noise with the Gaussian distribution. For internal noise, we assume it consists of equilibrium thermal fluctuations, which is a thermal noise with a white spectrum, although there may be other sources of noise, such as, $1/f$ noise, also known as brown noise. These sources can include induced signals from radio stations, mobile devices, TV stations, satellites, and so on. Despite working in a screened room, it is not possible to completely eliminate the effect of these noise sources.

4.4.1 External noise

A schematic representation of the stochastic signal and its corresponding probability distribution can be found in Fig. 4.17.
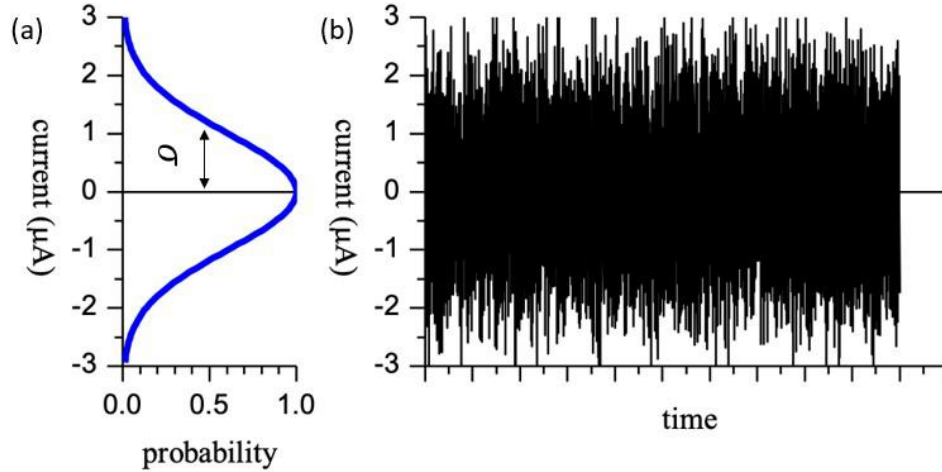
Figure 4.17: (a) The Gaussian distribution of probability of random signal with the width σ. (b) The random signal as function of time.

Our focus is on examining the impact of external noise through simulation. To accomplish this, we replace the deterministic ac-drive $I(t)$ with an external random signal to drive the ratchet in a stochastic regime. Since we are operating in the quasistatic regime, we again use the high-resolution experimental asymmetric IVC of A22 and numerically calculate all the characteristics.

To perform the calculation, we employ a similar procedure to the one used for the ac-drive. However, since we do not have a periodic signal, it is necessary to average voltage over a long (formally infinite) interval. Due to the ergodicity of the noise, we

can substitute the averaging over time by convolution with a Gaussian distribution, as outlined below,[3]

$$\overline{V}(\sigma, I_{dc}) = (V * G)(\sigma) = \int_{-\infty}^{\infty} V(I + I_{dc}) \cdot G(I, \sigma) \, dI,$$

where $G(I, \sigma)$ is the Gaussian distribution, which is defined as

$$G(I, \sigma) = \frac{1}{\sigma\sqrt{2\pi}} \exp\left(\frac{-I^2}{2\sigma^2}\right).$$

Similarly, we calculate $\overline{P}_{out}(\sigma, I_{dc}) = \overline{V}_{dc}(\sigma, I_{dc}) \cdot I_{dc}$, and

$$\overline{P}_{in}(\sigma, I_{dc}) = \int_{-\infty}^{\infty} V(I + I_{dc}) \cdot G(I, \sigma) \cdot I \, dI.$$

The numerically calculated $\overline{V}_{dc}$, $\overline{P}_{in}$, $\overline{P}_{out}$, and efficiency η of the noisy driven ratchet are presented in Fig. 4.18 and Fig. 4.19 respectively,
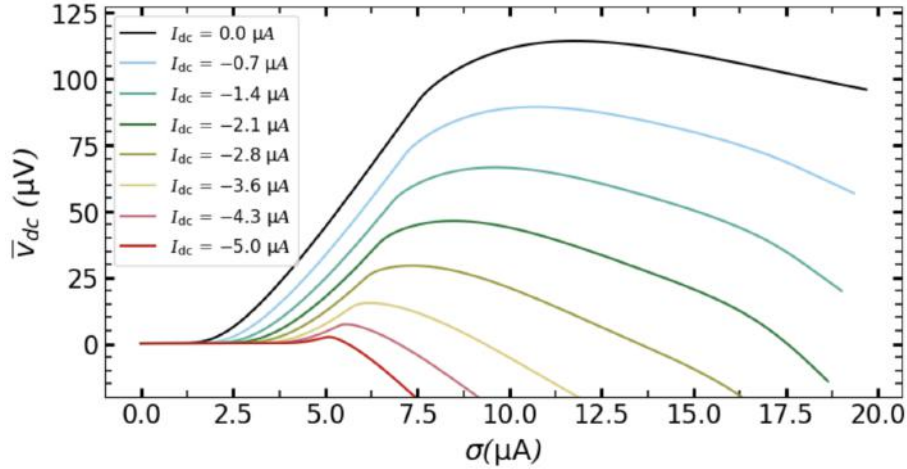
Figure 4.18: Numerically calculated $\overline{V}_{dc}(\sigma)$ based on experimental IVC.

---

[3]It is important to note that the amplitude of the Gaussian signal is infinite and random. Therefore, we adopt the parameter σ instead of I_{ac} as a measure of the amplitude of our noisy signal.
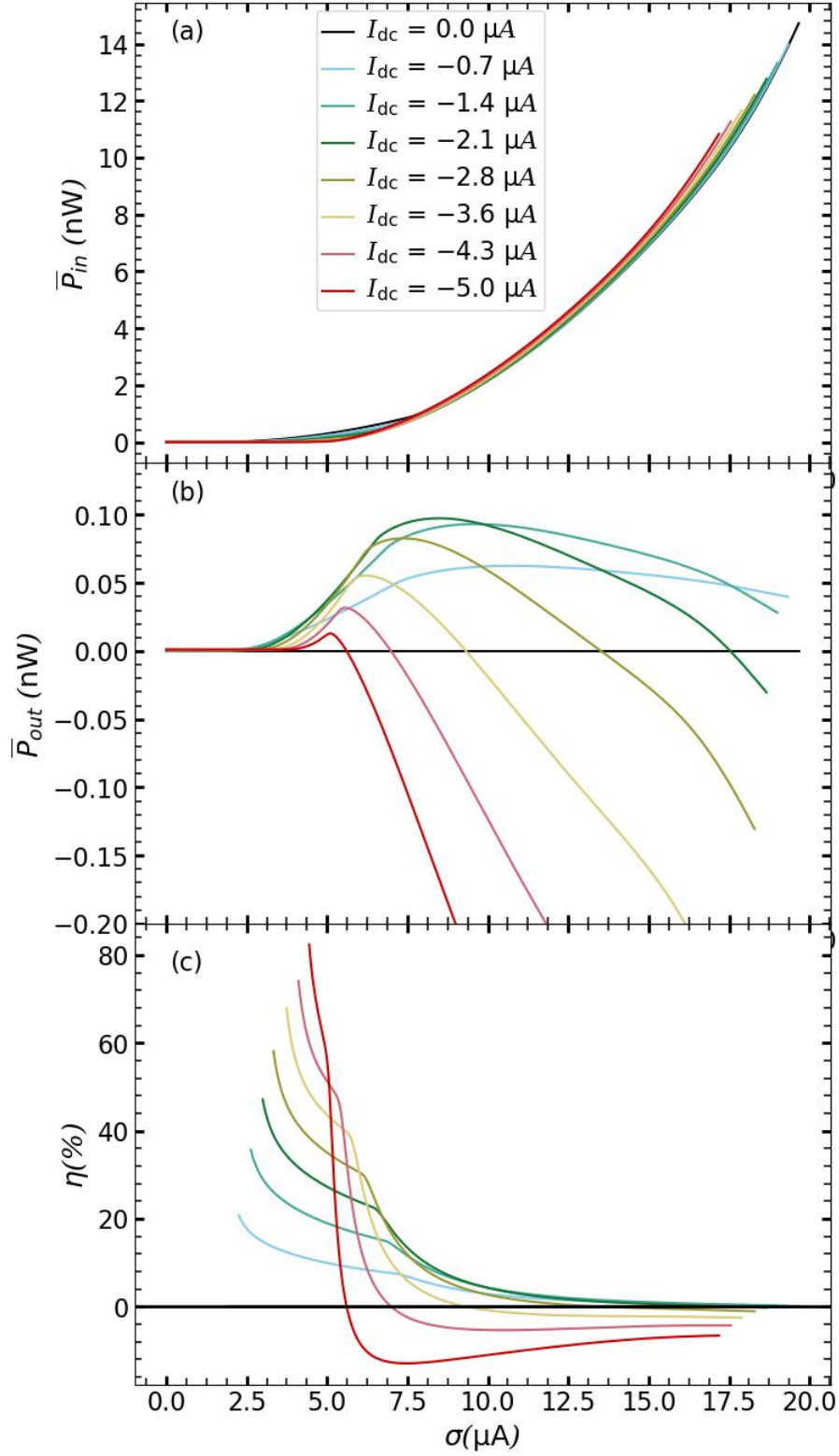
Figure 4.19: (a) $\overline{P}_{\text{in}}(\sigma)$. (b) $\overline{P}_{\text{out}}(\sigma)$. (c) Efficiency η for the ratchet driven by quasistatic Gaussian noise with amplitude σ.

We observe that our Josephson ratchet system remains functional when driven by a random signal instead of a deterministic drive. The figures of merit obtained under the random signal exhibit almost similar behavior to those achieved under the deterministic drive e.g., I_{stop} and the maximum efficiency are almost same as those for the deterministic values. However, the maximum value of the average voltage $\overline{V}_{\text{dc}}$, decreases by a factor of two compared to deterministic drive (ac-drive). Thus, the noise can still transport the particle, albeit at a slower pace.

4.4.2 Internal noise

For the case of internal noise, we utilize the intrinsic noise present within the system, commonly referred to as thermal noise. Thermal noise arises from the random fluctuations due to the thermal energy of the system, specifically in the shunt resistor at a finite temperature. These fluctuations exhibit an amplitude distribution that is nearly Gaussian. The fluctuation-dissipation theorem provides a generic and statistically derived explanation for this phenomenon in the field of statistical physics.

Due to the utilization of high-temperature superconductors (HTSs), our ratchet can be operated at temperatures up to around 40K where the the I_c of our JJs vanishes. At this temperature, the thermal energy $(k_B T)$ is approximately ten times greater compared to that at 4.2K. Consequently, the ratchet can be operated with a significantly higher thermal energy level. In the following we present the IVC of the ratchet A15 at a temperature around 4.2K and 35K.
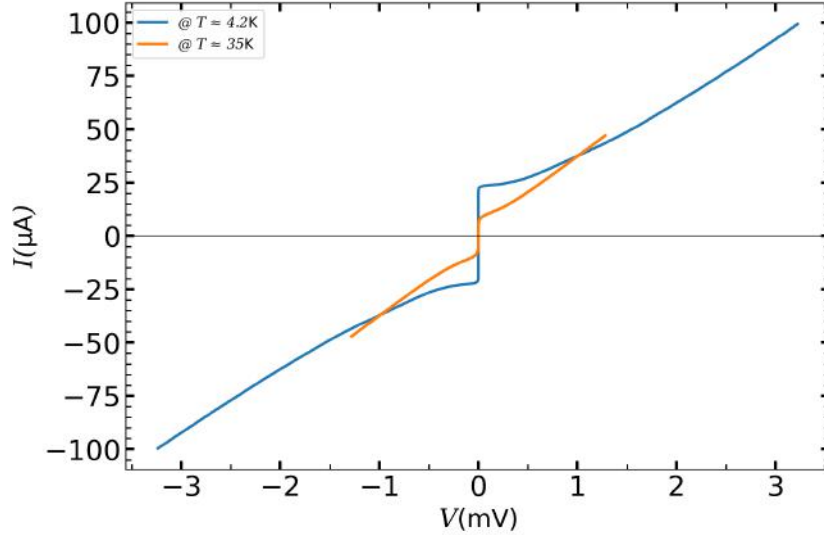

Figure 4.20: IVC of the ratchet A15 at $T \approx 4.2\,\text{K}$ and $35\,\text{K}$ at zero magnetic field $I_{\text{coil}} = 0$.

From Fig. 4.20 we observe that with increasing temperature, the critical current I_c decreases, while the thermal noise current

$$I_{\text{th}} = \frac{2\pi k_B T}{\Phi_0} \approx 1.4\,\mu\text{A}$$

increases at $T \approx 35$K. Consequently, as we approach temperatures in the range of 30-40K, we reach the point where thermal energy becomes comparable to the Josephson energy i.e., the thermal current becomes comparable to the critical current. Now, by applying the optimum magnetic field, we make I_{c_+} very small, smaller than the noise current, and therefore strongly smeared on IVC. The smearing of I_{c_+} can be characterized by the noise parameter Γ (see eq. (1.12)). [9] [13]

Now the key question is: will asymmetric IVC still cross the origin or not due to the rounding around I_{c_+}, e.g., one can get $V(0) \neq 0$. The IVC at $B = 0$ and at $B = B_{\text{opt}}$ at $T \approx 35$K is shown in Fig. 4.21. Upon zooming in, we confirm that the blue curve does not cross the origin. This indicates that the internal noise is rectified, producing a small dc voltage.
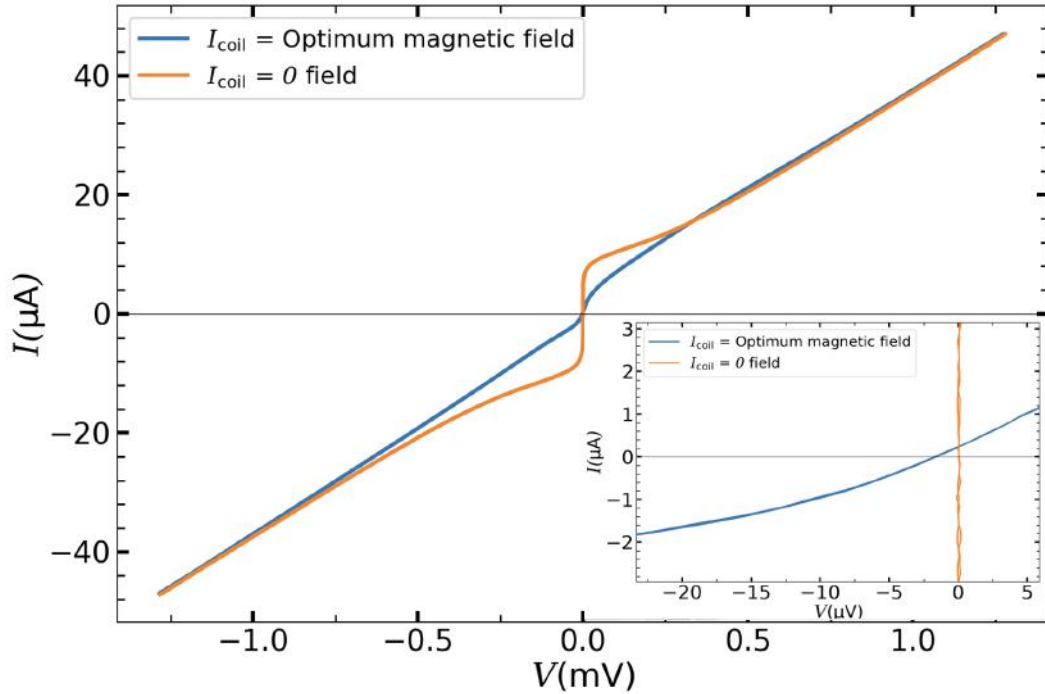
Figure 4.21: IVC for the ratchet A15 at around temperature 35K for the two values of I_{coil}: zero and the optimum magnetic field. In the lower right, we zoom in on the origin.

However, experimentally there can be many pitfalls. In particular, the lack of crossing origin may potentially be attributed to the shift of zero of the current source. To exclude this possibility, we disconnect the cable from the bias current source to the JJ, and perform the following measurement,
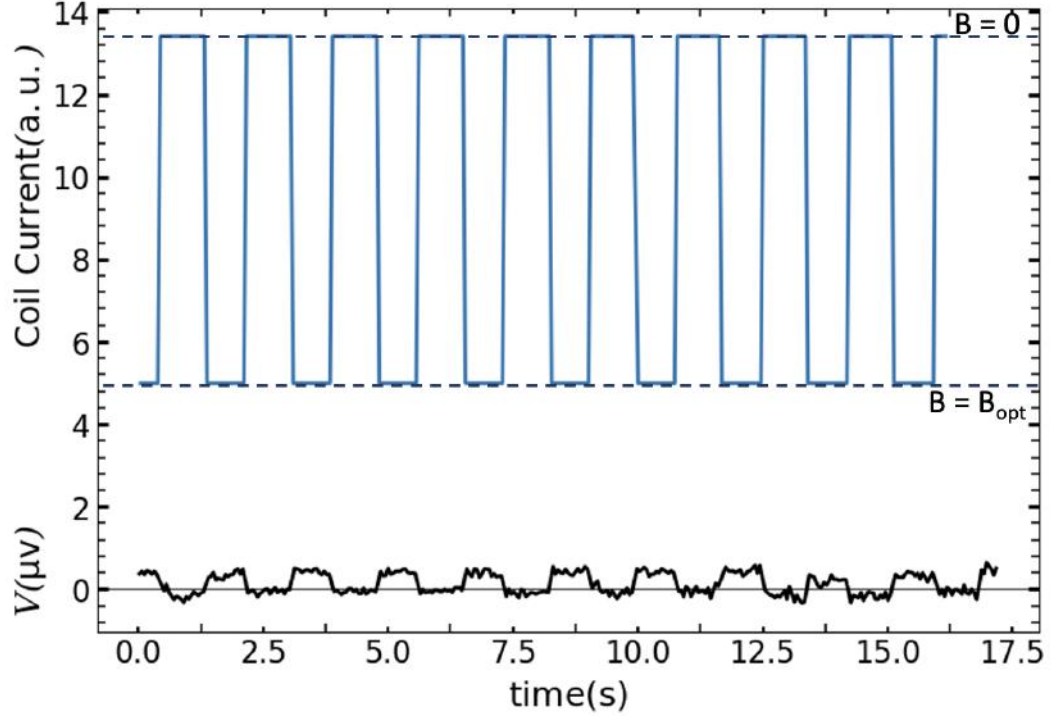
Figure 4.22

We recorded the voltage-versus-time $V(t)$ for device A15: while the coil current I_{coil} was switching between $I_{coil} = 0$ and its optimum value of $75\,mA$ quasi-statically, the results are shown in Fig. 4.22. It was observed that when $I_{coil} = 0$, there was no voltage response, indicating no rectification effect. However, for the optimum magnetic field, a voltage of approximately $0.4\,\mu V$ was observed. This voltage can be attributed to the rectification of noise. A similar effect was reported in a SQUID two decades ago [13].

However, it is known that the rectification of equilibrium thermal fluctuations (e.g., white noise) is prohibited by the second law of thermodynamics. Therefore, the rectification is probably related to some non-equilibrium noise, $1/f$ noise or induced signals from outside. The investigation of the spectral properties of the noise and its role in the rectification process will be a subject of future research and will be explored in forthcoming studies.

4.5 Conclusion and Outlook

Using He-FIB, we successfully fabricated the Josephson ratchet and demonstrated its remarkable performance: the efficiency up to 74% based on the asymmetry parameter $\mathscr{A} \approx 7$. The device achieved a maximum average rectified dc voltage $\overline{V}_{\mathrm{dc}} \approx 215\,\mu\mathrm{V}$, with a compact effective area of around $1\,\mu\mathrm{m}^2$. To the best of our knowledge, these results represent a record-breaking achievement in the field of Josephson ratchets, as demonstrated by the comparison in Table. 4.3.

Throughout this thesis, we conducted numerous measurements and simulations to investigate the behavior of the Josephson ratchet under both deterministic and stochastic driving conditions. Finally, we observed the effect of intrinsic noise on Josephson ratchet, which resulted in a small amount of rectified dc voltage$\sim 0.4\mu\mathrm{V}$ without any external drive at T$\approx$ 35K.

References	Type	$\mathscr{A}$	$\overline{V}_{\mathrm{dc}}(\mu\mathrm{V})$	$\overline{P}_{\mathrm{out}}(\mathrm{nW})$	$\eta(\%)$	Area ($\mu\mathrm{m}^2$)	$T_{\mathrm{op}}(\mathrm{K})$
Carapella (2001) [14]	ALJJ	1.2	5	-	-	44500	6.5
Beck (2005) [15]	ALJJ	2.2	20	-	-	5700	6
Sterck (2005) [16]	3JJ SQUID	2.5	25	-	-	43*	4.2
Sterck (2009) [13]	3JJ SQUID	2.2	25	-	-	1125†	4.2
Wang (2009) [17]	ALJJ	2.8	100	-	-	800	4.2
Knufinke (2012) [1]	ALJJ	1.6	40	16‡	25††	1300	4.2
Menditto (2016) [18]	φ junction	2.5	150	-	-	2000	1.7
Golod (2022) [3]	in-line JJ	4§	8	-	70††	7.2¶	7
Paolucci (2023) [19]	2JJ SQUID	3	8	-	6††	72‖	0.4
This thesis (2023)	in-line JJ	7	215	0.2	74	1**	4.2-35

Table 4.3: Comparison key parameters of Josephson ratchet from literature. ALJJ is the abbreviation of annular long JJ, and SQUID is the abbreviation of superconducting quantum interference device.

* The geometry (Fig. 1 of [16]) is not clearly presented in the paper, so we just summed up the area of the hole and the areas of three junctions.

† In Fig. 1(b) of [13], we roughly estimate the size of the device as 45×25 $\mu\mathrm{m}^2$.

‡ In [1], only $\overline{V}_{\mathrm{dc}}$ was measured. From Fig. 2 and Fig. 3, we determine that $I_{\mathrm{c}_-} = -0.5$ and $I_{\mathrm{c}_+} = 0.3$ in units of $I_0 = 2.8\mathrm{mA}$. We then find $I_{\mathrm{dc}}^{\mathrm{opt}} \approx -0.06$ corresponds to maximum $\overline{P}_{\mathrm{out}}$ from eq. (18), and substitute this value in eq. (17) to obtain maximum $\overline{P}_{\mathrm{out}}$. Note that, the units in eq. (17) are normalized. Therefore, to convert them to physical units, we multiply by $V_1 \cdot I_0 = 280\mathrm{nW}$, where $V_1 \approx 100\mu\mathrm{V}$.

§ This is the asymmetry at zero magnetic field. The authors claim that the asymmetry at the optimum magnetic field is ~ 10. In fact, in Fig 3(d) of [3] the asymmetry is around 8.

¶ We approximately calculate the area of the device as 6×1.2 $\mu\mathrm{m}^2$.

‖ From Fig. 2(a) of [19], we roughly estimate the area 6×12 $\mu\mathrm{m}^2$.

†† These efficiency values calculated for experimental asymmetry using the theoretical expression.

** The essential area we used for this work is 0.5×2 $\mu\mathrm{m}^2$, see Table. 4.1 and Fig. 3.12.

As an **Outlook**, we have several tasks in mind for future research. First, a more detail studies on the effects of noise is required. In particular, investigating the spectrum of the rectified signal and its bandwidth at different noise parameters. Since the influence of noise is subtle, to accomplish this, the fabrication of Josephson ratchets with smaller dimensions and shorter JJ length, while maximizing the asymmetry parameter $\mathscr{A}$, should be pursued.

Second, by achieving a significant number of well-performing ratchets (for example, by improving the quality of BJJs and minimizing the spread of j_c), one can construct an array of Josephson ratchets to obtain significant rectified dc voltage/power.

Third, one can develop a new generation of SQUIDs based on of the Josephson junction of in-line geometry with a periodic asymmetric potential. Surpassing the capabilities of simple Josephson junctions with symmetric potential and investigating the different probable effect of the periodic asymmetric potential into the system at nano scale.

These tasks represent exciting avenues for further exploration and advancement in the field of Josephson ratchets and related technologies.

References

[1] M. Knufinke, K. Ilin, M. Siegel, D. Koelle, R. Kleiner, and E. Goldobin. ″Deterministic Josephson vortex ratchet with a load″. Phys. Rev. E **85**, 011122 (2012).

[2] Peter Reimann. ″Brownian motors: noisy transport far from equilibrium″. Elsevier, **361**, Issues 2–4. (2002).

[3] Taras Golod and Vladimir M. Krasnov. ″Demonstration of a superconducting diode-with-memory, operational at zero magnetic field with switchable nonreciprocity″. Nature Comunication, **13**, 3658. (2022).

[4] E. Goldobin, R. Menditto, D. Koelle, and R. Kleiner. ″Model I–V curves and figures of merit of underdamped deterministic Josephson ratchets″. Phys. Rev. E **94**, 032203 (2016).

[5] Josephson effect. Wikipedia.

[6] Roderich Tumulka. ″Foundations of Quantum Mechanics″. Springer (2022).

[7] Ginzburg–Landau theory. Wikipedia.

[8] Antonio Barone and Gianfranco Paterno. ″Physics and applications of Josephson effect″, 1982.

[9] Dieter Kölle. ″Basic Properties of Josephson Junctions″. Koelle's Slides. (2019).

[10] Jodie Roderiguez. ″Characterization of Josephson junctions created by He$^+$ irradiation in commercial Ceraco $YBa_2Cu_3O_{7-x}$ thin films″, 2022. Bachelor thesis.

[11] B. Müller, M. Karrer, F. Limberger, M. Becker, B. Schröppel, C.J. Burkhardt, R. Kleiner, E. Goldobin, and D. Koelle. ″Josephson Junctions and SQUIDs Created by Focused Helium-Ion-Beam Irradiation of $YBa_2Cu_3O_7$″. Phys. Rev. Applied **11**, 044082 (2019).

[12] V. V. Dobrovitski V. G. Kogan, J. R. Clem, Yasunori Mawatari, and R. G. Mints. ″Josephson junction in a thin film. Phys. Rev. B **63**, 144501 (2001).

[13] Kleiner R. Sterck A, Koelle D. ″Rectification in a stochastically driven three-junction SQUIDs rocking ratchet″. Phys. Rev. Lett. **103**, 047001 (2009).

[14] G. Carapella and G Costabile. "Ratchet effect: Demonstration of a Relativistic Fluxon diode". Phys. Rev. Lett. **87**, 077002 (2001).

[15] M. Beck, E. Goldobin, M. Neuhaus, M. Siegel, R. Kleiner, and D. Koelle. "High-Efficiency Deterministic Josephson Vortex Ratchet". Phys. Rev. Lett. **95**, 090603 (2005).

[16] A. Sterck, R. Kleiner, and D. Koelle. "Three-junction SQUID Rocking Ratchet". Phys. Rev. Lett. **95**, 177006 (2005).

[17] H. B. Wang, B. Y. Zhu, C. Gürlich, M. Ruoff, S. Kim, T. Hatano, B. R. Zhao, Z. X. Zhao, E. Goldobin, D. Koelle, and R. Kleiner. "Fast Josephson vortex ratchet made of intrinsic Josephson junctions in $Bi_2Sr_2CaCu_2O_8$". Phys. Rev. B **80**, 224507 (2009).

[18] R. Menditto, H. Sickinger, M. Weides, H. Kohlstedt, D. Koelle, R. Kleiner, and E. Goldobin. "Tunable φ Josephson junction ratchet". Phys. Rev. E **94**, 042202 (2016).

[19] F. Giazotto F. Paolucci, G. De Simoni. "A gate- and flux-controlled supercurrent diode effect". Appl. Phys. Lett. **122**, 042601 (2023).